

MODELING OF EMISSION SIGNATURES OF MASSIVE BLACK HOLE BINARIES: I METHODS

TAMARA BOGDANOVIĆ^{1,2}, BRITTON D. SMITH, STEINN SIGURDSSON², AND MICHAEL ERACLEOUS²

Department of Astronomy & Astrophysics, Pennsylvania State University, University Park, PA 16802

Accepted by the Astrophysical Journal Supplements

ABSTRACT

We model the electromagnetic signatures of massive black hole binaries (MBHBs) with an associated gas component. The method comprises numerical simulations of relativistic binaries and gas coupled with calculations of the physical properties of the emitting gas. We calculate the UV/X-ray and the H α light curves and the H α emission profiles. The simulations are carried out with a modified version of the parallel tree SPH code *Gadget*. The heating, cooling, and radiative processes are calculated for two different physical scenarios, where the gas is approximated as a black-body or a solar metallicity gas. The calculation for the solar metallicity scenario is carried out with the photoionization code *Cloudy*. We focus on sub-parsec binaries which have not yet entered the gravitational radiation phase. The results from the first set of calculations, carried out for a coplanar binary and gas disk, suggest that there are pronounced outbursts in the X-ray light curve during pericentric passages. If such outbursts persist for a large fraction of the lifetime of the system, they can serve as an indicator of this type of binary. The predicted H α emission line profiles may be used as a criterion for selection of MBHB candidates from existing archival data. The orbital period and mass ratio of a binary may be inferred after carefully monitoring the evolution of the H α profiles of the candidates. The discovery of sub-parsec binaries is an important step in understanding of the merger rates of MBHBs and their evolution towards the detectable gravitational wave window.

Subject headings: black hole physics—galaxies:nuclei—hydrodynamics—line:profiles—radiation mechanisms:general

1. INTRODUCTION

Massive black hole binaries (hereafter MBHBs) may form as a result of several processes: through the breakup of a supermassive protostar (Begelman & Rees 1978), as a metastable state in the evolution of a cluster of massive objects (Saslaw et al. 1974; Bromm & Loeb 2003), and as a result of galactic mergers (Begelman et al. 1980; Valtaoja et al. 1989; Milosavljević & Merritt 2001; Yu 2002). The last mechanism is a major formation route for MBHBs and it relies on hierarchical merger models of galaxy formation (Haehnelt & Kauffmann 2002; Volonteri et al. 2003) and significant dynamical evidence that the majority of galaxies harbor massive black holes in their centers (e.g., Kormendy & Richstone 1995; Richstone et al. 1998; Peterson & Wandel 2000). In this paper we investigate observational signatures of MBHBs that result from galactic mergers.

Theoretical results imply that the evolution of a MBHB proceeds in three stages. In the first stage, the binary separation decreases through the process of dynamical friction when stars in the nuclear region are scattered by the binary. In the third stage, binary orbital angular momentum is efficiently dissipated via gravitational radiation emission and the binary proceeds to an inevitable merger. A possibility that in the second stage of evolution the binary merger stalls because of depletion of stars in the nuclear region, is still a topic of a lively scientific debate (Quinlan & Hernquist 1997; Sigurdsson 1998; Milosavljević & Merritt 2001; Hemsendorf et al. 2002; Merritt 2002; Yu 2002; Aarseth

2003; Milosavljević & Merritt 2003; Perets et al. 2006; Zier 2006). If this is indeed the case, binaries spend most of their lifetime at separations of 0.01 – 1 pc (Begelman et al. 1980) and the majority of observed binaries should be found in this evolutionary stage. Hereafter, we refer to this, second evolutionary stage in the life of a binary, as to *intermediate phase*.

A number of authors have suggested that interaction of a binary with a gaseous accretion disk may have significant effects on the inspiral and merger rates of MBHB (Ivanov et al. 1999; Gould & Rix 2000; Armitage & Natarajan 2002, 2005; Escala et al. 2004, 2005; Kazantzidis et al. 2005; Dotti et al. 2006a; Mayer et al. 2006a). It has been shown that massive gas disks tend to form in centers of merging galaxies (Barnes & Hernquist 1992, 1996; Mihos & Hernquist 1996). In particular, a gas disk may expedite the merger of a binary by dissipation of orbital angular momentum (Escala et al. 2004, 2005), reducing the merger time to $10^6 - 10^7$ yr.

Observationally, MBHBs may be identified directly in cases when a black hole pair is spatially resolved and when the separation and kinematic parameters point to a close, bound pair. In practice, there is only one such object identified so far: observations of NGC 6240, an ultra luminous infrared galaxy, with the *Chandra* X-ray observatory revealed a merging pair of X-ray active nuclei with a separation of 1.4 kpc (Komossa et al. 2003a). Recently Hudson et al. (2006) also reported on the X-ray detection of a wide, proto supermassive binary black hole at the center of cluster Abell 400. Practical obstacles in this type of direct identification arise for several reasons. Firstly, fairly high spatial resolution and accuracy in position measurements are required to resolve a binary active nucleus. The spatial resolution required to resolve an intermediate binary with orbital separation of 1 pc at the distance of ~ 100 Mpc is about 2 mas. With spatial resolutions currently

Electronic address: tamarab@astro.umd.edu, britton, steinn, mce@astro.psu.edu

¹ Current Address: Department of Astronomy, University of Maryland, College Park, MD 20742

² Center for Gravitational Wave Physics, Pennsylvania State University, University Park, PA 16802

achievable, it is easier to spot and resolve wide binaries, like NGC 6240, whereas it has been suggested that MBHBs spend a major fraction of their life time as intermediate, hard binaries (Begelman et al. 1980). Because of their high spatial resolution VLBA and VLBI radio observatories have a large potential for discovery of close binaries with separations of 0.1–10 pc, especially when combined with ground-based optical spectroscopic observations (Rodriguez et al. 2006).

The second most appealing piece of observational evidence for a MBHB would be a periodic manifestation of Keplerian motion. There are a handful of galaxies which exhibit periodicities in their light curves and thus can be considered as MBHB candidates (Fan et al. 1998; Rieger & Mannheim 2000; De Paolis et al. 2002, 2003; Sudou et al. 2003; Xie 2003). A prominent example is the blazar OJ 287 which exhibits outburst activity in the optical light curve with a period close to 12 years. The latest outburst of OJ 287, expected at the end of 2006, has not yet happened, putting to the test a number of models along with the binary hypothesis (Sillanpää et al. 1988; Lehto & Valtonen 1996; Valtaoja et al. 2000).

Another phenomenon associated with the existence of a MBHB is the change in the orientation of the black hole spin axis and its precession about the total angular momentum axis, caused by its interaction with another black hole (Merritt & Ekers 2002; Zier & Biermann 2001, 2002). This effect is one possible explanation for helical radio-jets, X-shaped, and S-shaped radio-jets, observed in some galaxies (e.g., Hunstead et al. 1984; Leahy & Williams 1984; Parma et al. 1985; Roos et al. 1993; Wang et al. 2003; Liu 2004), though alternative explanations are available (Capetti et al. 2002). In cases when the orbit of the less massive, inspiralling black hole becomes coplanar with an accretion disk of the primary, fueling of jets may be interrupted and re-started (Liu 2004). This could give rise to a second pair of jets aligned along the same axis with the initial pair, as seen in double-double radio galaxies (Schoenmakers et al. 2000; Liu, Wu, & Cao 2003).

Massive binary black holes may also influence the kinematics of the broad line region of the active galactic nucleus (AGN) which could be detected in periodic variations of broad emission lines (Begelman et al. 1980; Gaskell 1983). Gaskell (1996) suggested that double peaked emission lines originate in binary broad line regions. In this scenario periodic velocity shifts of each peak in the line profile should reflect the orbital motion of a single broad line region associated with one of the black holes. After extensive spectroscopic monitoring of MBHB candidates spanning two decades the predicted long term periodic variability was not confirmed, leaving little room for a binary broad line region scenario (Halpern & Filippenko 1988, 1992; Eracleous et al. 1997). Eracleous et al. (1997) noted that perturbation of a single broad-line region by a second MBH is still an open possibility, and in fact the only good interpretation for some objects. Another version of this hypothesis in which the secondary black hole perturbs the broad line region of the primary was offered by Torres et al. (2003) as an explanation of the variable Fe K α line in 3C 273. Etherington & Maciejewski (2006) suggest that characteristic spiral arm morphology can arise within the inner 1 kpc of a gas disk as a consequence of perturbations in a binary potential, and that in the absence of more direct techniques, this signature may be used for a MBHB search.

Another, soon-to-be-opened observational window should allow detection of gravitational waves from MB-

HBs (Thorne & Braginskii 1976; Centrella 2003; Baker 2003). These are expected to be an important class of sources for the Laser Interferometer Space Antenna, *LISA* (Bender 1998; Danzmann 1996; Haehnelt 1994; Hughes 2002; Wyithe & Loeb 2003; Sesana et al. 2004, 2005; Rhoads & Wyithe 2005). Since it is not clear which model should be used to describe the optical data (binary orbital motion or disk and jet precession), the masses of current candidate binary systems are highly uncertain. The future data from gravitational radiation observations, combined with information on optical counterparts, should play an important role in determining the most likely scenario (Komossa 2003b; Armitage & Natarajan 2005). In a broader sense, once enough information about the statistical properties of such binaries is available, it should be possible to constrain the merger rates and merger histories of massive and super-massive black hole binaries (Haehnelt 1994; Menou et al. 2001; Hughes 2002). For this reason a large scientific effort has been recently directed towards understanding the electromagnetic signatures in different pre-merger and post-merger phases of MBHBs (Milosavljević & Phinney 2005; Kocsis et al. 2006; Dotti et al. 2006b). The work we present in this paper fits within this broader context.

In §2 we present our method for calculation of emission signatures of MBHBs. The results are described in §3, the discussion and future prospects in §4, and in §5 we give our conclusions.

2. NUMERICAL SIMULATIONS

We have carried out smoothed particle hydrodynamical (SPH) simulations of the binary and a gaseous component, and we have characterized the physical properties of the gas by calculating heating, cooling, and radiative processes as an integral part of simulations. Based on these results we have calculated the accretion-powered continuum and H α light curves, as well as the H α emission line profiles emerging from the inner parts of a gas disk on a scale of < 0.1 pc.

For the first time we attempt to model both gas and binary dynamics in the nuclear region on sub-parsec scales in order to bridge the gap between large scale hydrodynamic simulations of merging galaxies and numerical relativity simulations of the late, pre-coalescence evolutionary phase in the life of a binary. The binary-gas evolution in simulations of merging galaxies has been followed down to separations of > 0.1 pc (Dotti et al. 2006c). The simulations that reach even smaller separations are computationally expensive, mostly because they need to be carried out at high resolution in force (or equivalently time). Additionally, if the nuclear processes followed include accretion, then a high resolution in mass is desired as well. These requirements are combined with the wide spatial and temporal dynamic range set by the nature of the problem itself. For the above reasons, in our simulations we focus on the length scale occupied by a nuclear accretion disk and do not consider the disk structure on larger scales.

We have used a modified version of *Gadget* (Springel et al. 2001; Springel 2005) to carry out the MBHB simulations. *Gadget* is a code for collisionless and gas-dynamical cosmological simulations. It evolves self-gravitating collisionless fluids with a tree *N*-body approach, and collisional gas by SPH. *Gadget* was not originally intended to carry out relativistic calculations. For this reason we have performed several modifications to the code in order to treat the two massive black holes relativistically. We have introduced the black hole particles as collisionless massive particles

with pseudo-Newtonian potentials. The calculations with a pseudo-Newtonian potential account for the decay of a black hole binary orbit through emission of gravitational radiation (§2.2). The gravitational drag from gas particles on the two black holes is accounted for through a contribution from every gas particle to each black hole's acceleration.

We set up the two Schwarzschild black holes as sink particles and model the accretion rate of gas and resulting accretion luminosity. The approach in which a black hole is treated as a sink particle has been introduced before in simulations of star formation (Bate et al. 2003; Li et al. 2005) and accretion onto supermassive black holes (Springel et al. 2005). In our model, a particle is considered to contribute to the unresolved accretion flow near a black hole once it crosses the hole's accretion radius, R_{acc} . R_{acc} is set to a fiducial value of $20 r_g$, comparable to the smallest length scale resolved in the simulation (i.e., the smoothing length of particles in a region of high density, $h_{sml} \sim 10 r_g$, where $r_g \equiv GM_{BH}/c^2 = 1.48 \times 10^{13} M_8 \text{ cm}$, and $M_{BH} = 10^8 M_8 M_\odot$ is the mass of a black hole). Once the gas particles find themselves within R_{acc} their dynamics is not temporally resolved. This choice allows to avoid a simulation hang-up when the integration time step of such particles becomes very small. We introduce a numerical approximation in the calculation of the accretion rate in order to account for the fact that the unresolved accretion flow of particles inside R_{acc} radius is noisy and that their dynamics cannot be described by the model of a steady accretion disk. Because of the short dynamical time associated with the innermost region of the accretion disk the particles there respond quickly to the variable potential of the binary which causes the streams of gas to collide and intersect with each other. From the total amount of gas that crosses R_{acc} in given time dt , only a fraction of the gas will be accreted, while the rest will gain enough momentum to avoid accretion onto the black hole. The accretion rate of a noisy flow of particles across some radius r is in general case proportional to the surface area, $\dot{M} \propto r^2$, assuming the planar and uniform distribution of particles within r . We calculate from the simulations the rate with which particles cross R_{acc} and extrapolate from it the accretion rate of particles that would have crossed the Schwarzschild radius as $\dot{M}(2r_g) \approx \dot{M}(R_{acc}) (R_{acc}/2r_g)^{-2}$. The estimate obtained in such way is conservative as we do not take into account the gravitational focusing by the black holes, which would increase the flow of particles towards the black holes and thus, their accretion rates. In § 4, we discuss the effect of our assumptions about the accretion model on the observational signatures.

2.1. Viscosity

The viscosity is parametrized in numerical calculations in order to account for the transfer of momentum and angular momentum without detailed assumptions about the nature of the phenomenon. One widely used parametrization is based on the Shakura-Sunyaev model (Shakura & Sunyaev 1973), where the α -parameter takes values less than 1.0, and typically $\alpha \leq 0.1$. Starling et al. (2004) for example find $0.01 \leq \alpha \leq 0.03$, for accretion disks in AGN, based on the observed continuum variability. Finding a suitable parametric description for the viscosity in SPH calculations which would faithfully describe the angular momentum transfer in different physical regimes has been a major issue over many years (Hernquist & Katz 1989; Monaghan 1992; Balsara 1995; Steinmetz 1996; Monaghan 1997; Springel

2005). A notable improvement in the treatment of viscosity was offered by parametrization that perform better in conserving the entropy of a simulated system (e.g., in *Gadget-2*; Springel 2005). Although we have used the version of *Gadget* released earlier (Springel et al. 2001), for the purposes of our calculations we adopted the viscosity prescription given in the new version of the code, *Gadget-2*. The physical properties in our simulations that are directly affected by this choice are the accretion rate of gas onto black holes and the internal energy of the gas – both of which play very important roles in the observational appearance of the system.

We derive the value of the artificial viscosity parameter used in the code, α_{Gadget} in such way that it corresponds to the Shakura-Sunyaev viscosity parameter $\alpha < 1$. We note that this relation is only a convenient way of describing the viscosity numerically and should not be interpreted as a statement about the physical viscosity in the disk. In SPH simulations, the viscosity acts as an excess pressure which is assigned to particles in the equation of motion, $P \approx \alpha_{Gadget} (c_s \omega - \frac{3}{2} \omega^2) \rho$, where c_s is the speed of sound and ω is the relative velocity of the two approaching particles. We compare this to the Shakura-Sunyaev tangential stress component $P \approx -\alpha c_s^2 \rho$, and obtain a local relation between the parameters describing a single particle interaction

$$\alpha \approx \alpha_{Gadget} \left(-\frac{\omega}{c_s} + \frac{3}{2} \frac{\omega^2}{c_s^2} \right). \quad (1)$$

The resulting artificial viscosity as described by equation (1) does not explicitly depend on the density of gas particles. However, in simulations a major increase in internal energy due to viscous dissipation occurs in high density regions which are conducive to high rate of particle interactions (i.e., collisions). The implication is that the relation connecting the two viscosity parameters depends on the density of gas particles in a simulation, namely,

$$\alpha \approx \alpha_{Gadget} \left(-\frac{\omega}{c_s} + \frac{3}{2} \frac{\omega^2}{c_s^2} \right) \left(\frac{\rho}{\rho_o} \right)^2, \quad (2)$$

where $\rho = \rho(r)$ is the density distribution of gas particles and $\rho_o = \rho(r_{in})$ is the value of the density at the inner radius of the accretion disk. Assuming that the largest value that ω can take is of the order of particle orbital velocities one can find a value of α_{Gadget} which corresponds to some value of the Shakura-Sunyaev α . From equation (2) we find that in order to have $0.01 \leq \alpha \leq 0.1$, at radial distances $\xi \sim 100$ from a black hole, in a disk where $c_s \sim 100 \text{ km s}^{-1}$, we have to choose $\alpha_{Gadget} \approx 10^{-6}$. Hereafter, we use ξ as the radius in units of gravitational radii ($\xi = r/r_g$).

2.2. Elliptical Orbits in the Paczynsky-Wiita Potential and Gravitational Wave Emission

We choose a pseudo-Newtonian Paczynsky-Wiita potential (Paczynsky & Wiita 1980) to describe the potentials of massive black holes in our calculations

$$\psi = \frac{-GM_{BH}}{(r - r_s)}, \quad (3)$$

where $r_s = 2GM_{BH}/c^2$. The two black holes can initially be placed on circular or elliptical orbits. The properties of circular orbits in the Paczynsky-Wiita potential are described in Paczynsky & Wiita (1980). In addition, we derive expressions

for the orbital velocity of a test particle on an elliptical orbit in the Paczynsky-Wiita potential in order to assign initial velocities consistent with the potential. We adopt the reduced two-body problem parametrization where $M = m_1 + m_2$ and $\mu = m_1 m_2 / (m_1 + m_2)$, where the energy and angular momentum of a system are calculated with respect to its center of mass (m_1 and m_2 are masses of the two black holes). We start with the requirement that in the Paczynsky-Wiita potential, the total energy and orbital angular momentum at the pericenter and apocenter of the orbit are equal. This leads to the following conditions:

$$v_p^2 - v_a^2 = 2GM \left(\frac{1}{r_p - r_s} - \frac{1}{r_a - r_s} \right), \quad (4)$$

$$r_p v_p = r_a v_a, \quad (5)$$

where v_p , v_a , r_p , and r_a are the velocity and radial distance of the reduced mass body, μ , at the pericenter and apocenter, respectively. From equations (4) and (5) we derive the velocity at the pericenter as

$$v_p = \sqrt{\frac{2GM}{r_a + r_p} \frac{r_a^2}{(r_p - r_s)(r_a - r_s)}}. \quad (6)$$

From the expression for the orbital angular momentum, $L/\mu = r_p v_p = r^2 \dot{\theta}$ (where r is the radial distance of the reduced mass from the center of mass of the system, and θ is its true anomaly), we find the angular azimuthal velocity.

$$\dot{\theta} = \frac{1}{r^2} \sqrt{\frac{2GM}{r_a + r_p} \frac{r_a^2 r_p^2}{(r_p - r_s)(r_a - r_s)}}. \quad (7)$$

We derive the radial velocity component from the equation of an ellipse, $r = a(1 - e^2)/(1 - e \cos \theta)$,

$$\dot{r} = \frac{dr}{dt} = \frac{dr}{d\theta} \dot{\theta} = -\frac{e \sin \theta r^2 \dot{\theta}}{a(1 - e^2)}. \quad (8)$$

Using the equation (6) and the condition $E(r_p, v_p) = E(r, v)$ we find the *vis viva* expression for an elliptical orbit in the Paczynsky-Wiita potential to be

$$v = (2GM)^{1/2} \times \left(\frac{1}{r - r_s} + \frac{1}{r_p - r_s} \frac{1}{(r_a/r_p)^2 - 1} - \frac{1}{r_a - r_s} \frac{1}{(r_p/r_a)^2 - 1} \right)^{1/2} \quad (9)$$

As the binary orbits in Paczynsky-Wiita potential it loses a fraction of its energy and orbital angular momentum through gravitational wave emission. We assume that as the binary contracts by emission of gravitational waves, the two black holes remain on elliptical orbits. This assumption is justified in our simulations where the total mass of the gas in a simulation is much smaller than the mass of a binary. Consequently, the perturbations of the elliptical orbits of black holes by the underlying gas distribution are small.

Following Landau & Lifshitz (1975) we calculate the rate of the energy loss to gravitational radiation using the quadrupole approximation

$$\frac{dE}{dt} = -\frac{32G\mu^2\Omega^6 r^4}{5c^5}, \quad (10)$$

where $\Omega(r)$ is the orbital frequency in the Paczynsky-Wiita potential. From this equation it is possible to obtain the radiation reaction acceleration at the center of mass frame of the

binary (Lee & Kluźniak 1999, and references therein)

$$\vec{a} = -\frac{1}{\mu} \frac{dE}{dt} \frac{\vec{v}}{v^2}. \quad (11)$$

chosen so as to preserve the symmetry of forces acting on each member of the system. This requirement ensures that the total momentum of the system is conserved while the individual components recoil due to the emission of gravitational waves.

2.3. Heating and Cooling of the Gas

We have investigated two different scenarios for radiative heating and cooling, assuming the emitting gas can be described as a black-body (BB) or a solar metallic-gas. The option for radiative heating and cooling of hydrogen-helium gas is also implemented in the code, following Thoul & Weinberg (1996), Black (1981), Cen (1992), and Katz et al. (1996), but was not used in the runs reported here. The cooling scenarios are mutually exclusive and by comparing them one can study the importance and impact of various cooling mechanisms in our simulations. In our simulations, the gas is heated by shocks and “external” sources of illumination. We assume that the sources of illumination are powered by accretion onto the massive black holes. After accretion on either of the two black holes becomes significant, UV and soft X-ray radiation emitted from the innermost portion of the accretion flow photo-ionizes the gas. The bolometric luminosity of an accretion-powered source of ionizing radiation can be written as:

$$L_{acc} = \eta \frac{GM_{BH} \dot{m}}{2r_s} = \frac{1}{2} \eta \dot{M} m_p c^2 \quad (12)$$

where $\eta = 0.01$ is the assumed radiative efficiency, \dot{m} and \dot{M} are the mass and particle accretion rates, respectively, and m_p is the mass of a gas particle.

1. Black-body case.

In this scenario, the illuminated gas absorbs and emits the radiation as a black-body. Each gas particle is therefore treated as an optically thick cell of gas, in local thermal equilibrium within a radius equal to its smoothing length, h_{sml} . A fraction of the incident energy absorbed by the gas depends on a coverage factor of the gas ζ , i.e., the fraction of solid angle covered by gas, as seen from the position of a source, and the distance of an absorbing gas cell from the source, r . From our simulations we find $\zeta \sim 10^{-4}$, corresponding to a fraction of particles exposed to illumination from an external source at any given time. We do not take into account radiation pressure, i.e., the momentum that is transferred to the gas particles by the incident radiation. We write the expression for the heating rate of the gas per unit volume as

$$\Gamma_{bb} = \frac{1}{2} \zeta L_X \frac{\rho}{m_p} \left(\frac{h_{sml}}{r} \right)^2 \text{ erg cm}^{-3} \text{ s}^{-1}. \quad (13)$$

Here we assume that L_X is the portion of the accretion luminosity carried by ionizing photons ($L_X/L_{acc} \approx 0.1$). The black-body cooling rate per unit volume is evaluated from the Stefan-Boltzmann equation and it can be written as

$$\Lambda_{bb} = 4\pi h_{sml}^2 \sigma T^4 \frac{\rho}{m_p} \text{ erg cm}^{-3} \text{ s}^{-1}, \quad (14)$$

where σ is the Stefan-Boltzmann constant.

2. Solar metallicity gas.

Spectroscopic observations of AGN show a wide range of metal absorption and emission lines, implying that most AGN systems are metal-rich. Additionally, metals are important coolants under the physical conditions typically found in AGN broad line regions. Therefore, in order to correctly model and describe these systems it is necessary to also include metals as constituents of the gas. However, detailed calculations of radiative transfer, coupled with parallel hydrodynamic simulations present a large computational challenge and are currently not possible. Including metals in heating and cooling calculations results in a large network of equations, especially if non-LTE processes are included. The solution of the heating and cooling equations dominates the CPU usage in a parallel hydrodynamics code to the extent that the calculation becomes prohibitively expensive.

Here we describe the approximate method we used for calculation of heating and cooling of the gas with metals. We have constructed a number of cooling maps using the photoionization code *Cloudy* (Ferland et al. 1998). Since the maps are used in computationally expensive numerical calculations, it is impractical to call *Cloudy* every time a cooling rate is needed. Instead, we pre-calculate a grid of cooling maps over a wide range of parameters, where the range of parameters has been determined from preliminary calculations without cooling. The parameter grid is read in by the simulation code, and radiative heating and cooling rates are linearly interpolated from the existing grid points. The cooling maps are calculated in the parameter space of *density* and *temperature* of the gas and *intensity* of ionizing radiation. The range of parameter values for which the maps were computed is as follows: $10^9 \text{ cm}^{-3} < n < 10^{19} \text{ cm}^{-3}$, $2000 \text{ K} < T < 10^8 \text{ K}$, and $0 \text{ erg cm}^{-2} \text{ s}^{-1} < J < 10^{17} \text{ erg cm}^{-2} \text{ s}^{-1}$. Because one of the assumptions in *Cloudy* is that the electrons are non-relativistic, the present range of its validity extends to temperatures below roughly 10^9 K . Gas at higher temperatures than this is commonly encountered in our simulations; in such cases we calculate heating and cooling rates by linearly extrapolating the grid values. In the SPH simulations we set the lower threshold for the gas temperature to 100 K and assign no upper threshold. The calculation in *Cloudy* is explicitly one dimensional, with results depending only on the depth coordinate. Propagation of line photons is conducted using the escape probability approximation. In this approach the escape probability for a photon is calculated under the assumption that the difference between the mean intensity averaged over the line and the source function at some location in the emitter is due to photons leaking away from the region (Ferland 2003). Although this approximation is used in many state-of-the-art plasma codes because of its computational facility, it is not known to what extent it affects predictions of the line intensities.

The density and temperature of the gas are evaluated in the SPH simulation after every time step. The spectral energy distribution (SED) of the ionizing radiation is

taken to be a power-law with an index $\alpha = 1$, extending from $\nu_1 = 1.36 \text{ eV}$ to $\nu_2 = 100 \text{ keV}$, a distribution commonly assumed for the central engines of AGN.

$$J_\nu = J_0 \left(\frac{\nu}{\nu_0} \right)^{-\alpha} \text{ erg cm}^{-2} \text{ s}^{-1} \text{ Hz}^{-1}, \quad (15)$$

where ν_0 is some arbitrarily chosen frequency and $J_0 = J(\nu_0)$ is the normalization of a SED that can be directly evaluated from the luminosity of an accretion source, eq. (12), as follows

$$F_{acc} = \frac{\zeta L_{acc}}{4\pi r^2} = \int_{\nu_1}^{\nu_2} J_\nu d\nu \approx 11.2 J_0 \nu_0, \quad (16)$$

where F_{acc} is the total flux incident on the gas cell located at the distance r from the ionizing source. In addition to the cooling processes included in *Cloudy* we also consider Compton cooling from a thermal distribution of non-relativistic electrons, which may become a significant coolant for the hottest and densest gas in the nuclear region.

$$\Lambda_{Comp} = 4.48 \times 10^{-5} \left(\frac{T}{10^9 \text{ K}} \right) \left(\frac{n_e}{10^{10} \text{ cm}^{-3}} \right) \times \left(\frac{F_{acc}}{10^{10} \text{ erg cm}^{-2} \text{ s}^{-1}} \right) \text{ erg cm}^{-3} \text{ s}^{-1}, \quad (17)$$

where n_e is the electron number density. When information about the cooling rate per unit volume, $\Lambda_k = \Lambda_{Cloudy,k} + \Lambda_{Comp,k}$, is obtained for every gas particle k in the simulation, their internal energy is modified accordingly. Thus, the heating and cooling are directly coupled with the evolution of the physical conditions in the gas. The total cooling rate from the gas (i.e., the bolometric luminosity) is obtained by summing over all particles, $\sum_{k=1}^{N_{part}} \Lambda_k (m_p / \rho_k)$. We do not assume that the gas is in thermal equilibrium, and consequently cooling is not necessarily balanced by heating. The integration scheme used in implementation of cooling for both the black-body and solar metallicity models is explicit. The cooling time for individual gas particles in our simulations is typically longer than the time step assigned based on their acceleration, $dt \propto 1/a_p$, and the Courant condition. Even when the cooling time is very short, $dt \leq 10^2 \text{ s} < t_{cool}$, guarantying the numerical stability of the integration. In all of the calculations the default abundance pattern is assumed to be solar. The atomic species considered by *Cloudy* range from hydrogen to zinc.

Since *Cloudy* includes a detailed treatment of radiation processes, we have also used it to calculate the $H\alpha$ line intensity and optical depth, the electron scattering optical depth, and the neutral hydrogen column density for each gas cell. As we will describe in the next section this information allowed us to relax some of the important assumptions commonly used to calculate the $H\alpha$ light curves and emission line profiles.

2.4. Calculation of $H\alpha$ light curves and emission line profiles

We chose the Balmer series $H\alpha$ line ($\lambda_{rest} = 6563 \text{ \AA}$) to describe the emission signatures of a MBHB. The broad $H\alpha$ line is thought to reflect the kinematics of the gas in the

TABLE 1
MODEL PARAMETERS

M_1 (M_\odot)	M_2 (M_\odot)	M_{disk} (M_\odot)	ψ	P_{orb}^b (yr)	a^b (r_g)	e^b	θ^b ($^\circ$)	α_G^c	η^d	ξ_{in} (r_g)	i ($^\circ$)	ϕ_0 ($^\circ$)
10^8	10^7	10^4	PW ^a	15.7	3007	0.7	0 (30 ^e)	10^{-6}	10^{-2}	10^2	30	0

^a PW = Paczynsky-Wiita potential; equation (3).

^b The initial values of binary orbital parameters.

^c Viscosity parameter; equations (1) and (2).

^d Radiative efficiency; equation (12).

^e in case of counter-rotating binary (SR) model only.

broad line region of AGN (Sulentic et al. 2000), and it is typically found to emerge from a wider range of radii in the broad line region than the UV and X-ray band broad emission lines (e.g., Eracleous et al. 1996; Wandel et al. 1999; Sulentic et al. 2000). Also, the H α line is the most prominent broad line in the optical spectrum and the least contaminated by the neighboring narrow emission lines. It is mostly powered by illumination of a disk by an emission source (Collin-Souffrin & Dumont 1989). The emission sources in our simulations are the innermost regions of the accretion flow around the two massive black holes that give rise to ionizing UV and soft X-ray radiation (Shakura & Sunyaev 1973). The cool gas is optically thick to the incident UV/X-ray photons which can escape the disk only after they have been converted to photons of lower energy. One portion of the absorbed UV/X-ray radiation is reprocessed by the gaseous disk and re-emitted as the broad H α line (Shakura & Sunyaev 1973, see their discussion of broad recombination and resonance emission lines).

The most important consideration in calculating the emitted H α light is the efficiency with which the gas reprocesses the incident ionizing radiation and re-emits it in the H α band. This efficiency is commonly characterized by the surface emissivity of the gas. The emissivity of the photoionized gas depends on numerous physical parameters. Locally, it depends on the physical properties of gas. Globally, its spatial distribution depends on the structure and morphology of the accretion disk. The H α emissivity can be most accurately assessed with photoionization calculations, thus we used this approach in the case of a *solar metallicity* gas.

In cases when photoionization calculations are not available, the emissivity is often parametrized as a function of radius, $\epsilon = \epsilon_0 \xi^{-q}$, where $q \approx 3$. This is justified by the photoionization calculations of Collin-Souffrin & Dumont (1989), which suggest that the emitted H α flux is approximately proportional to the incident continuum flux for a wide range of values of the density and column density. We have compared the emissivity determined from our own photoionization calculations with the parametric model (Figure 1) and found a qualitative agreement between the two. We also notice a significant amount of scatter in the emissivity values from the photoionization calculation, which is expected due to variations in surface density of the perturbed gas disk in our model.

Once the surface emissivity of each gas cell in the simulation is known, the H α luminosity can be expressed as $L_{\text{H}\alpha} \propto \sum_{k=1}^{N_{\text{part}}} \epsilon_k$, where k is a particle index. The implicit assumption, following from the above luminosity expression, is that the gas is optically thin to H α photons. We find this assumption to be justified for a cold disk since its optical depth to H α light is less than 10^{-4} . We show the optical depth of

gas cells to the H α photons as a function of the disk radius in Figure 2. When the gas is exposed to an intense ionizing continuum, the optical depth to the H α photons increases significantly because many hydrogen atoms are in the first excited energy state. However, in our profile calculations we do not correct for the absorption of the H α photons by the gas. This is because we are not able to correct consistently for absorption of photons along the line of sight with the numerical code we have used. The effects of our assumptions on the H α luminosity and emission line profiles are discussed in § 3.5 of the text.

The H α emission line profiles have been calculated taking into account the relativistic Doppler shift, $v_{\text{obs}} = v_{\text{rest}} \sqrt{1 - \beta^2} / (1 + \beta \cos \theta)$, and the gravitational redshift in the potential well of a Schwarzschild black hole, $v_{\text{obs}} = v_{\text{rest}} \sqrt{1 - 2/\xi}$, where v_{obs} and v_{rest} are the observed and rest frequencies of an emitted photon, β is the velocity of an emitter in units of speed of light, and θ is an angle between the direction of motion of an emitter and the observer's line of

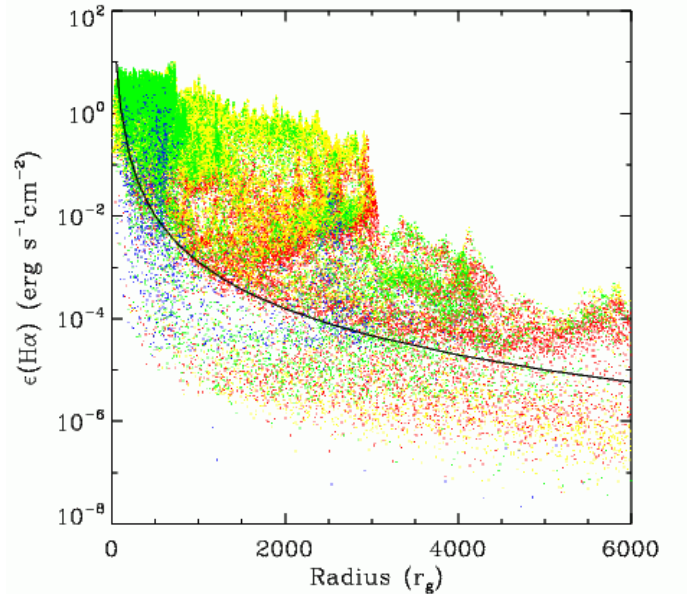


FIG. 1.— H α emissivity of the gas as a function of radius, at 9.4 years for a model with solar metallicity gas. The emissivity of each gas cell plotted in the figure is weighted by the density of the gas at that position, so that comparison with the parametric emissivity model (plotted as a solid line with arbitrary normalization) can be made. The temperatures of gas particles are marked with color: red $T < 10^4$ K; yellow $10^4 \text{ K} < T < 10^6$ K; green $10^6 \text{ K} < T < 10^8$ K; blue $10^8 \text{ K} < T < 10^{10}$ K; and violet $T > 10^{10}$ K. This figure corresponds to the morphology of the disk plotted in panel 2 of Figure 7.

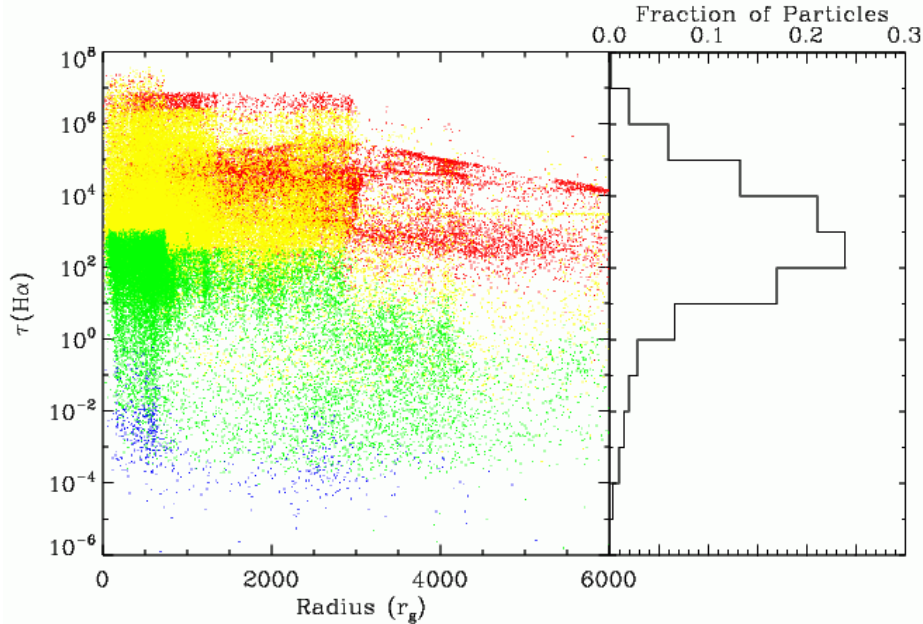


FIG. 2.— *Left:* Optical depth of gas cells to H α photons as a function of radius at 9.4 years for a model with solar metallicity gas. The color legend is the same as in Figure 1. This figure corresponds to the morphology of the disk as shown in panel 2 of Figure 7. *Right:* Histogram showing the fraction of particles as a function of $\tau(\text{H}\alpha)$.

sight. In the next section we summarize our choice of parameters used in SPH simulations as well as the calculation of light curves and line profiles.

2.5. Choice of Parameters

In the calculations presented here, both black holes are treated as massive particles in the pseudo-Newtonian Paczynsky-Wiita potential. The masses of the primary and secondary black holes, together with the other parameters are shown in Table 1. In all simulations the binary mass ratio is chosen to be 0.1.

Based on current theoretical and observational understanding of MBHBs it is not obvious what kind of orbits the binaries have in the intermediate phase of their evolution. The resulting accretion rate and observational signature of a MBHB depend sensitively on the shape and orientation of its orbit with respect to the gas disk. The astrophysical significance of a predicted signature depends on the longevity of the particular phase in the life of a binary and consequently on the probability that binaries will be detected in that evolutionary phase (MacFadyen & Milosavljević 2006). The recent simulations of Dotti et al. (2006a) imply that binaries which co-rotate with the gaseous disk circularize and loose the memory of their initial orbital eccentricity. On the other hand, counter-rotating binaries tend to preserve their original eccentricity down to ≈ 1 pc, a limit set by the resolution of their simulation. In addition, simulations of gas disks with planets suggest that under some conditions tidally perturbed eccentric disks can excite the eccentricity in a binary and that the two are coupled (Papaloizou, Nelson, & Masset 2001). Very few constraints on the type of orbit can be placed from the observations. An exception is the MBHB candidate OJ 287, for which it has been suggested that the binary orbit with an eccentricity of 0.7–0.8 and orbital period close to 12 yr is coplanar with the accretion disk (Sillanpää et al. 1988; Valtaoja et al. 2000; Liu & Wu 2002).

In the calculations presented here the primary and secondary black holes are moving on elliptical orbits. At the

beginning of a simulation the black holes start from the apocenters of their orbits (except in the model where the secondary starts with a true anomaly of $\theta = 30^\circ$, see § 3.3). The initial values of the semi-major axis and eccentricity are $3007 r_g$ and 0.7, respectively. The period of the binary, calculated at the beginning of the simulation is 15.67 yr.

The accretion disk is initially only associated with the primary black hole. It is coplanar with the binary orbit and it extends from $\xi_{in} = 100$ to $\xi_{out} = 2000$ (ξ_{out} translates to 0.01 pc in physical units, a size expected for AGN nuclear accretion disks). The mass of the disk is $10^4 M_\odot$ and the number of gas particles in the disk is 10^5 . The mass of the thin disk is constrained by the requirement that its surface density be in the range that is commonly found in AGN broad line regions, where the broad H α emission line is expected to originate. In addition, the disk mass is roughly consistent with the results of the larger scale simulations (Escala et al. 2005; Dotti et al. 2006a; Mayer et al. 2006a), where the mass of the gas disk enclosed within central 1 pc is of the order of the mass of the binary. Extrapolating from these results and assuming a constant surface density for simplicity, one obtains a disk mass of $\sim 10^4 M_\odot$, for a disk size of 0.01 pc and a $\sim 10^8 M_\odot$ binary. In § 4, we discuss how the choice of the disk mass may affect the observational signatures.

The initial rotational velocities of gas particles were calculated based on the gravitational forces only while the effect of pressure was neglected in initially cold and unperturbed disk. We choose the initial temperature of the disk to be $T = 2000$ K everywhere. The initial surface density distribution in the disk is $\Sigma \propto \xi^{-1.5}$, as set by the requirement that the disk has a uniform vortensity (defined as the ratio of vorticity to surface density). This criterion must be satisfied in order to construct the equilibrium model of an infinitesimally thin gaseous disk. The initial conditions have been chosen in such way that the disk remains near hydrostatic equilibrium before the secondary black hole plunges into it. Figure 3 shows the evolution of the disk surface density and temperature profile,

TABLE 2
RESULTS

Model	Cooling	N_{part}	Duration (yr)	t_{peri}^a (yr)	Density ^b (cm^{-3})	c_s^b (km s^{-1})	$L_{H\alpha}^c$ (erg s^{-1})
BB	black-body	100k	37	8, 23	$10^7, 10^{12}$	$5, 10^3$...
S	solar	100k	36	8, 23	$10^8, 10^{13}$	$5, 10^2$	$\sim 10^{40}$
SR	solar	100k	32	3, 18	$10^8, 10^{13}$	$5, 10^2$	$\sim 10^{40}$
S1	solar	20k	50	8, 23, 38	$10^8, 10^{13}$	$5, 10^2$	$\sim 10^{40}$
S2	solar	20k	38	8, 23, 38	$10^8, 10^{13}$	$5, 10^2$	$\sim 10^{40}$
IC1	solar	20k	8	...	10^{13}	5	...
IC2	solar	100k	8	...	10^{13}	5	...
IC3	solar	500k	8	...	10^{13}	5	...

^a Approximate times of pericentric passages.^b Median value for the low and high density component. IC runs: median value for the unperturbed disk.^c Estimated peak luminosity.

from the initial conditions run with 100k particles (IC2) before the secondary black hole is introduced. The gas in the IC2 run is assumed to have a solar metallicity. The temperature of the disk settles around 1000 K in this period and there are no visible transients. No boundary conditions were applied at the inner and outer edge of the disk in our simulations.

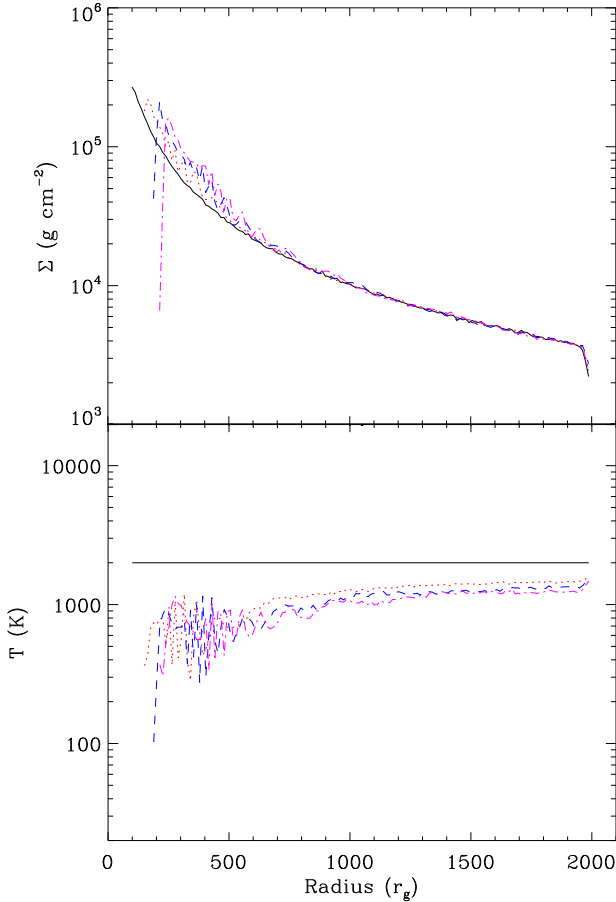


FIG. 3.— Evolution of the disk surface density and temperature profile before the secondary black hole is introduced into the simulation (IC2 run). The profiles correspond to progressively longer times as follows: 0 years (solid, black line), 2.2 years (dotted, red line), 4.4 years (dashed, blue line), and 6.6 years (dash-dot, purple line) after the beginning of the simulation.

Figure 3 shows a gradual evolution of the disk edges towards the regions of low density. This is a consequence of the fact that the disk has sharp edges, where particles are subjected to asymmetric pressure forces. We do not expect the diffusion of particles from inner edge towards the primary black hole to affect the results, since no particles are accreted during this initial period. At later times, in runs where the secondary interacts with the disk, the contribution to the accretion rate from a slow diffusion process should be negligible in comparison with the total accretion rate induced by the interactions.

The viscosity parameter, radiative efficiency, and metallicity of the gas are kept constant, as described above; their values can be found in Table 1. The softening parameter, ξ_{soft} , used in the expression for force in order to avoid numerical singularity, ranges between 0.1 and 0.2 (in units of M_8) for gas particles and is 4.0 for the massive black holes.

We compute line profiles emerging from the gaseous disk under the assumption that the observer is located at a distance $d \rightarrow \infty$, in the positive xz -plane, at $i = 30^\circ$ to the z -axis. Changing the inclination, changes the values of the projected velocities (i.e., the overall width of the line profile) but has a relatively small effect on its shape otherwise. The azimuthal orientation of the observer is an additional parameter in the modeling of non-axisymmetric systems. The azimuthal orientation is measured in the orbital plane of a black hole binary, counter-clockwise with respect to the positive x -axis. In the calculations we present here, we adopt $\phi_0 = 0^\circ$ as an arbitrary direction towards the observer.

3. RESULTS

We present and compare results of three different scenarios in which the evolution of a massive black hole binary and coplanar gaseous accretion disk is followed over two orbital periods of the binary (~ 30 years in total). The simulations span only two orbits because at the temporal resolution required by the hydrodynamical calculation, we find it computationally expensive to follow a binary over many orbital periods. The calculation of the two orbits, with total of 10^5 particles, required about 20 days of CPU time on 8 2.8GHz Intel Xeon processors per simulation. We find that 50-70% of the CPU time is consumed by the hydrodynamic calculations, including the neighbor search, density determination, computation of hydro forces, and heating and cooling of the gas. A fraction of 20-30% of the CPU time is spent on computation of gravitational forces, including the tree walks and

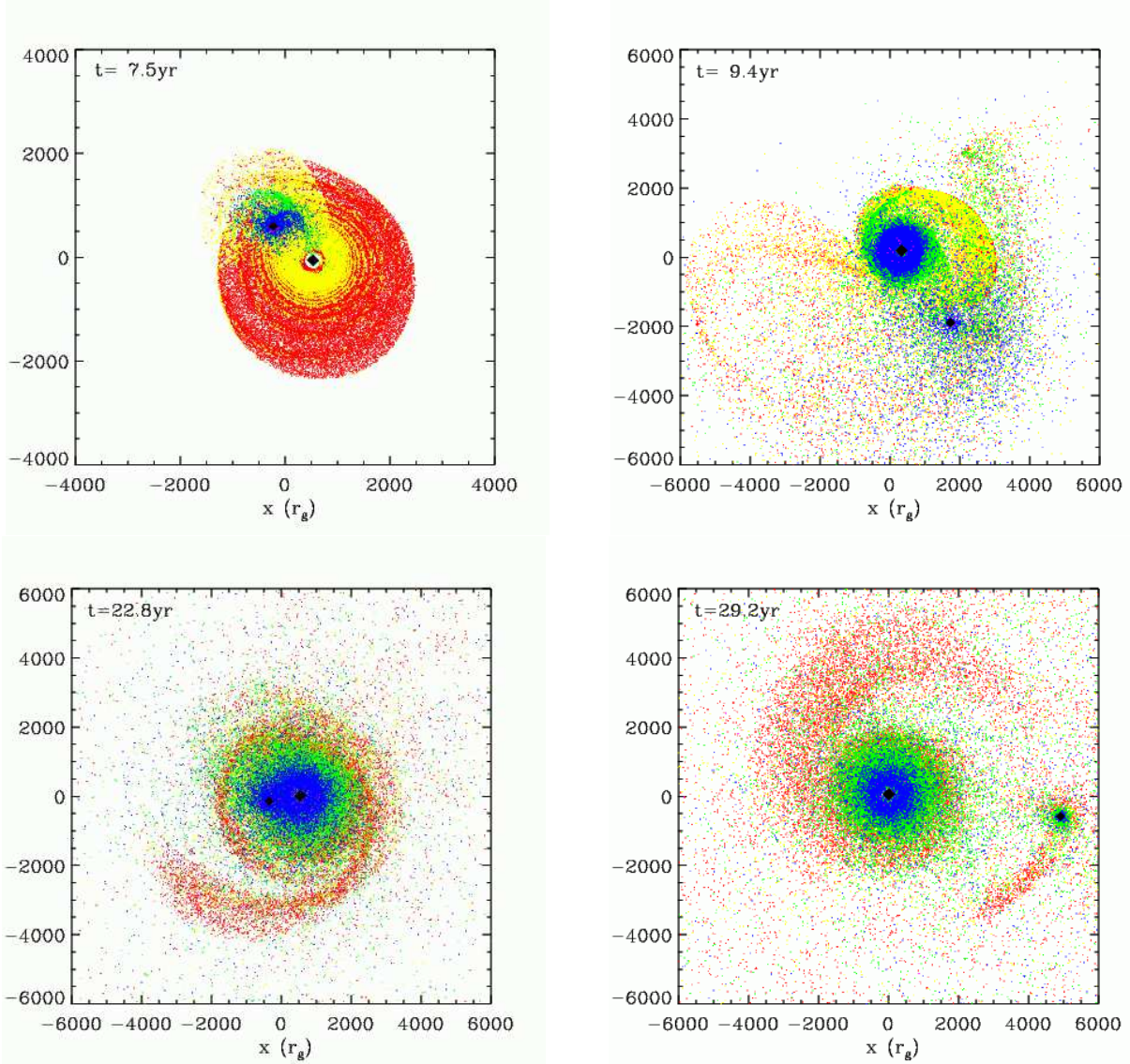


FIG. 4.— Sequence of snapshots from the simulation showing the evolution of the binary and gas in the BB-model (projected into the plane of the binary orbit). The time stamp is marked on the top of each panel. The first snapshot shows the system shortly after the secondary plunges into the disk for the first time. The rotation of the binary and the disk is counter-clockwise. The color legend is the same as in Figure 1. Note that higher temperature particles are plotted over the lower temperature ones, with the result that some information is hidden.

tree construction. We find 8 CPUs to be an optimal number of processors in terms of speed for calculations that employ 10^5 particles. Increasing the number of processors as 2^n (i.e., to 16, 32, etc.) results in a loss of computational speed because the CPU time consumption becomes dominated by the communication among the processors.

In the first of three calculated scenarios the binary is co-rotating with the accretion disk which is assumed to absorb and emit radiation as a *black-body*. In the second and third scenario the binary is co-rotating and counter-rotating with respect to the disk, respectively, and the gas is assumed to have a *solar metallicity*. In the last two cases the heating and cooling of gas are followed with photoionization calculations.

3.1. Co-Rotating Case With Black-Body Cooling (BB-model)

The approximation in which emission from a geometrically thin accretion disk is represented by a modified black-body spectrum has been widely utilized since the work of Shakura & Sunyaev (1973). We use this simple model as a control case for our simulations and we compare it with the photoionization models.

Before the plunge of the secondary black hole into the disk the density in the quasi-steady disk ranges between 10^{15} and 10^{12} cm^{-3} at the innermost and outermost edges of the disk, and in the intermediate region it takes values according to the assumed power-law surface density. The temperature of the quiescent disk quickly adjusts to a two phase distribution. The higher density gas, which occupies the inner portion of the disk cools more efficiently (eq. 14) and reaches a temperature of $\sim 10^2 \text{ K}$ (Fig 4). The lower density gas occupies a distinct phase in temperature space at $\sim 10^3 \text{ K}$. We are not able to follow the phase of steady accretion at low rates prior

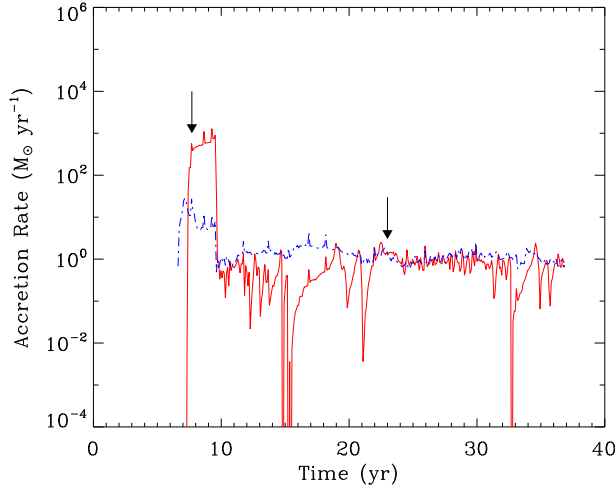


FIG. 5.— Effective accretion rate onto the primary (solid, red line) and secondary (dashed, blue line) black holes calculated from the BB-model. The accretion rate curves can be translated into UV/X-ray light curves, by assuming that $1 M_{\odot} \text{ yr}^{-1}$ produces $\sim 10^{43} \text{ erg s}^{-1}$ of UV/X-ray luminosity. The arrows mark the times of pericentric passages of the binary.

to the impact of the secondary. This is because our accretion disk is initially set with an inner edge at $\xi_{in} = 100$, where viscous migration of gas in the radial direction is slow. For the set of parameters we have adopted, the theory of steady thin disks predicts an accretion rate of $10^{-4} - 10^{-3} M_{\odot} \text{ yr}^{-1}$. The unperturbed disk is stable to gravitational collapse as determined by the value of the Toomre parameter, $Q = c_s \Omega / G \Sigma$, where Ω is the angular speed of the gas and Σ is its surface density. The innermost region of the gas disk has the lowest Toomre parameter, of order of a few but consistently larger than 1. The speed of sound, $c_s = (\gamma p / \rho)^{1/2}$, also shows a characteristic two phase distribution with values lower than 10 km s^{-1} across the disk, where $\gamma = 5/3$ for a mono-atomic, ideal gas. The physical properties of the disk remain stable and do not change over a considerable period of simulation time, until the secondary black hole plunges into it. This is an indication that the disk has settled into a quasi-steady state and that any further physical changes can be attributed to the interactions with the binary.

The tidal perturbation by the secondary causes the disk to become eccentric and develop a spiral pattern, even before the secondary plunges into it. The physical properties of the disk are significantly altered after the plunge, which occurs ~ 6 years after the beginning of the simulation. The secondary forms a shock where the temperature persists at 10^{12} K . While in this model the cooling of the gas is less efficient, there is no doubt that the shock has formed and that it trails behind the secondary as it travels through the disk.

In our model, a source of illumination is assumed to turn on once the accretion onto a black hole begins. With both black holes accreting there are two sources illuminating and heating the gas. As a result a portion of the gas is blown out of the plane of the disk and forms a hot “corona”. The temperature of the gas is highest in the vicinity of the black holes, where it is in the range of $10^6 - 10^{10} \text{ K}$. After the first passage of the secondary the disk has formed a single trailing spiral which cools radiatively and adiabatically to $T \sim 10^3 \text{ K}$ (Fig 4). The secondary black hole acquires a small, gravitationally bound corona of gas from the disk. After the second

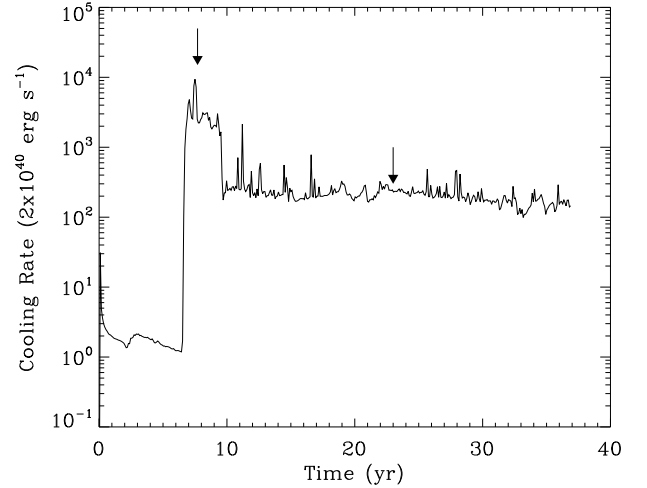


FIG. 6.— Cooling rate of the gas as a function of time calculated from the BB-model. The cooling rate shown here traces the bolometric light curve of the gas disk (the power generated locally in the disk). The arrows mark the times of pericentric passages of the binary.

passage the secondary further heats and perturbs the disk gas which now reaches the scale of a parsec in the plane of the disk (recall the disk initial size 0.01 pc). The secondary black hole intersects the spiral arm of the disk and gravitationally captures a portion of it. For a while, the secondary moves on its orbit followed by the remainder of the spiral arm, which resembles a cometary tail. Since a large portion of the spiral arm, which retains a significant amount of colder gas in the disk, is disrupted after the second orbital passage, the effective temperature of the gas becomes more dominated by the inner hot portion of the disk. The morphology of the system at the completion of the second binary orbit consists of a discernible denser disk component immersed into a spherical halo of tenuous gas. The gas density now spans the range from $10^{10} - 10^{13} \text{ cm}^{-3}$ in the disk component and it extends down to 10^5 cm^{-3} in the low density regions on the scale of $\sim 1 \text{ pc}$. The speed of sound is $\sim 5 \text{ km s}^{-1}$ and $\sim 10^3 \text{ km s}^{-1}$ for the cold and hot gas phases, respectively (Table 2).

During the two orbits the accretion rate onto the two black holes is highly variable. The secondary black hole starts accreting soon after the plunge and is followed by the primary which starts accreting a year later at a much higher, super-Eddington rate $\dot{M} \sim 10^3 M_{\odot} \text{ yr}^{-1}$ (Fig 5). The jump in accretion rate is caused by a sudden increase in outward angular momentum transport in the disk triggered by a gravitational perturbation of the disk by the secondary. We observe such a high accretion rate in this simulation only. This happens because the high density gas in the central portion of the disk in the BB cooling model initially equilibrates at lower temperatures than in the photoionization models. The cold gas with a very low velocity dispersion is more easily driven towards the primary black hole when the secondary reaches the pericenter, at the end of year 7 of the simulation. The second pericentric passage of the secondary occurs 23 years after the beginning of the simulation. During the second passage there is no large increase in the accretion rate because the gas has acquired a significant amount of internal energy and additional kinetic energy and it is not easily swept up by the secondary. The accretion rates onto the primary and secondary black holes become comparable later in the simulation. Unlike the sec-

ondary, the primary black hole exhibits large variations in the accretion rate (~ 2 orders of magnitude). This occurs because the primary black hole accretes colder gas, confined to the plane of the disk, while the secondary black hole accretes from the hotter, more uniform halo as it sweeps through it, in a process resembling Bondi-Hoyle accretion. If the accretion continues at the mean rate derived from the first two orbits the disk mass would be exhausted in only ~ 300 years. In order for accretion to persist the accretion disk needs to be continually replenished by an external supply of gas.

The cooling rate of the gas closely follows the heating rate (Fig 6), corresponding to a bolometric luminosity of the gas of $\sim 10^{43} \text{ erg s}^{-1}$. The bolometric luminosity as a function of time does not exhibit large fluctuations and remains at a nearly constant value after the first 10 years of binary evolution. In the BB-model the luminosity of the accretion powered sources dominates over the bolometric luminosity of the gas disk (i.e., the power locally generated in the disk) by at least one order of magnitude during the period of “uniform” accretion and by several orders of magnitude during the first pericentric passage. This is a consequence of inefficient radiative cooling (compared to photoionization calculations). In the BB model, the inefficient radiative cooling is compensated by adiabatic expansion of the gas, resulting in a more pronounced spatial dispersion of the gas.

3.2. Co-rotating Case with Solar Metallicity Gas (S-Model)

Figure 7 shows the evolution of the morphology and temperature of gas at the same times as Figure 4. The initial steady state disk in the solar metallicity model (hereafter, the S-model) has a temperature of $\sim 10^3 \text{ K}$ and does not exhibit the “two phase” temperature distribution, seen in the BB-model. The speed of sound in the unperturbed disk is about 5 km s^{-1} . The bolometric luminosity of the gas disk during this period is powered by collisional excitation only and it is of order $10^{40} - 10^{41} \text{ erg s}^{-1}$ (Figure 9).

The gas in the S-model shows the same main morphological features as in the BB-model. The differences between the two are that after the interaction with the secondary the gas in the S-model remains cooler and shows less dispersion with the result that the spiral arm and filaments are more pronounced. Because of the way we plot particles in Figure 7 (higher temperature particles are plotted over the lower temperature ones), part of the information remains hidden. For a better illustration, in Figure 8 we plot the temperature distribution in the disk as a function of radius which shows that multiple temperature components can be present at a single radius. The disk density at the end of the simulation is in the range $10^{10} - 10^{14} \text{ cm}^{-3}$, and the median density is about one order of magnitude higher than in the BB-model (see Table 2). The disk gas in this model also remains well above the Toomre threshold for gravitational instability. The speed of sound is about 5 km s^{-1} in the cold disk and $\sim 10^2 \text{ km s}^{-1}$ in the hotter gas component. The temperature of the gas reaches the highest value ($T \sim 10^{12} \text{ K}$) after the shock is formed by the secondary. On a time scale of months, the temperature of the gas falls below 10^{10} K due to the combined effects of radiative cooling and adiabatic expansion. The dominant radiative cooling mechanisms of the shocked gas are inverse Compton and free-free emission. The hot component of the gas spends a significant amount of time in the temperature range $10^4 - 10^8 \text{ K}$. In this regime the radiative cooling is dominated by free-free emission and recombination radiation, while in-

verse Compton emission becomes inefficient in comparison. On the other hand, the cold component of the gas, confined to the spiral arm, has the same physical properties as that in the BB-model and it retains a temperature of $10^3 - 10^4 \text{ K}$.

In the period before the impact of the secondary, the radiative cooling rate of the solar metallicity gas matches that of the BB-model (Figs 6 and 9). This is an important test of the S-model, because steady, geometrically thin disks are indeed expected to be optically thick and behave as a black-body. The differences in the cooling processes between the S-model and the BB-model appear after the (accretion-powered) sources of ionizing radiation turn on. The gas in the S-model exhibits less efficient heating and more efficient cooling relative to the BB-model. This happens because the ionized gas remains optically thin to ionizing radiation and absorbs it less efficiently, while at the same time free-free and recombination cooling processes are boosted. Once the gas has been ionized its physical properties depart from these in the black-body model.

After the first pericentric passage of the secondary the accretion rate reaches $10 M_{\odot} \text{ yr}^{-1}$ (Figure 10), comparable to the Eddington rate for this system, $\dot{M}_E \approx 30 M_8 (\eta/0.01)^{-1} M_{\odot} \text{ yr}^{-1}$. During the remainder of the simulation the accretion rate remains at a nearly constant level of about $1 M_{\odot} \text{ yr}^{-1}$. This implies that the accretion luminosity is just below the Eddington luminosity ($L_E = 1.51 \times 10^{46} M_8 \text{ erg s}^{-1}$) for a few years after the first pericentric passage of the binary and later settles at luminosity $\sim 10^{-2} L_E$. During this period the bolometric luminosity of the disk, powered by shocks and illumination, is found to be $\sim 10^{45} \text{ erg s}^{-1}$ on average, with fluctuations of up to 2 orders of magnitude. The bolometric luminosity of the gas disk is comparable to that of the photoionization sources. Additionally, the pericentric passages, in the 7th and 23rd years of the simulation, can be easily discerned in the cooling curve (Figure 9). These are not noticeable in the cooling curve of the BB-model (Figure 6) because its bolometric luminosity is dominated by emission from the diffuse gas component. A common property of the BB and S-models is large fluctuations in the accretion rate of the primary, a consequence of the accretion of cold gas. Moreover, the largest dips in the accretion rate of the primary coincide with the apocentric passage, when the gas is tidally pulled away from the primary and the primary exhibits the slowest orbital motion.

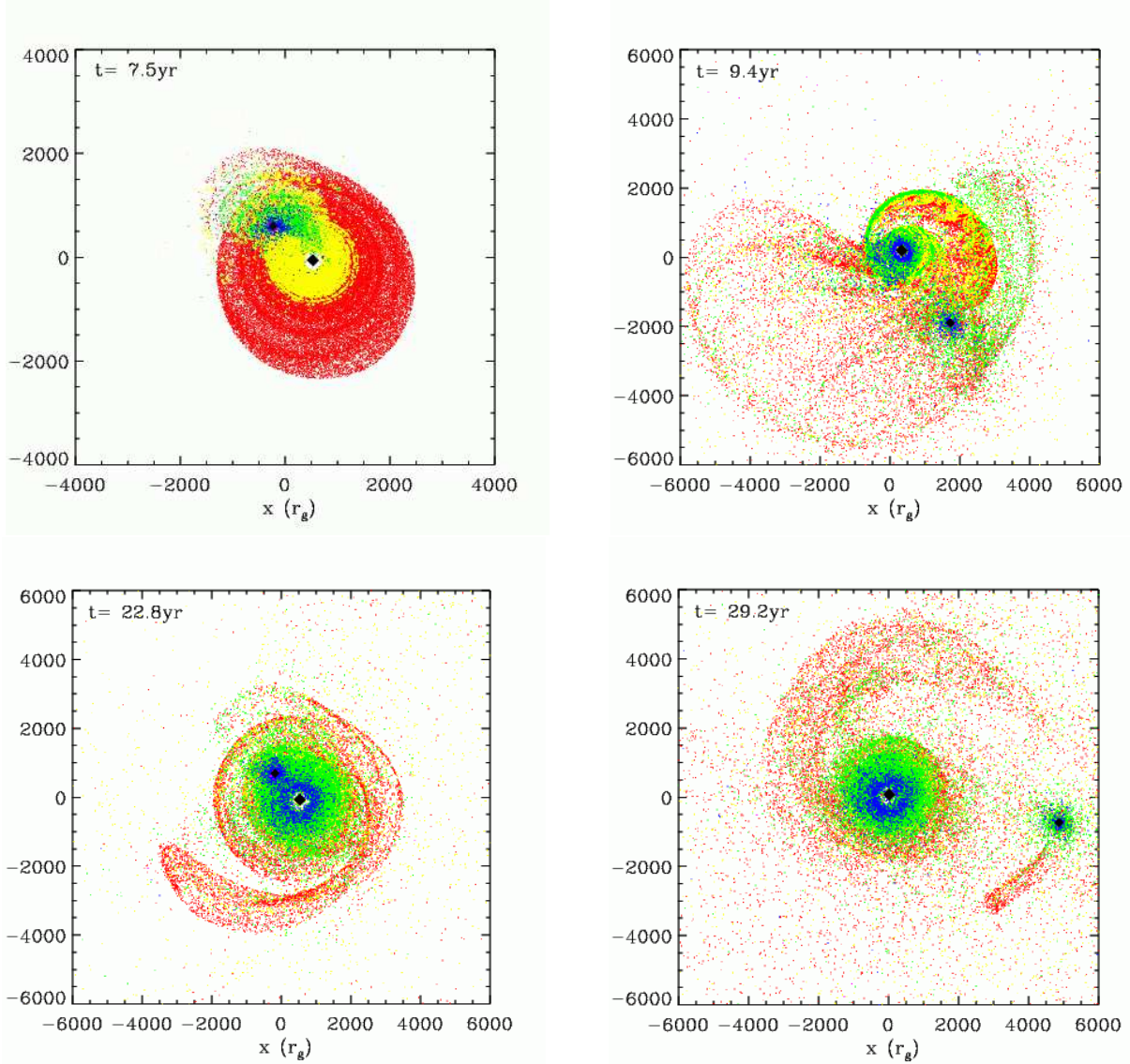


FIG. 7.— Sequence of snapshots from the simulation showing the evolution of the binary and gas in the S-model (projected into the plane of the binary orbit). The time stamps are marked on the top of each panel and are the same as in Figure 4. The first snapshot shows the system shortly after the secondary plunges into the disk for the first time. Note that the second pericentric passage in the S-model occurs about 100 days later than in the BB-model. The rotation of the binary and the disk is counter-clockwise. The color legend is the same as in previous figures. The higher temperature particles are plotted over the lower temperature ones, with the result that some information is hidden (see Figure 8).

3.3. Counter-rotating Case With Solar Metallicity Gas (SR-Model)

In this scenario the binary and gas disk rotate in opposite directions with respect to each other. In Figure 11 we show the morphology and the temperature distribution, while in Figure 12 we plot the temperature stratification in the disk for this model at a single time. During the pre-plunge phase the physical properties of the disk are comparable with those in the co-rotating S-model. The plunge of the secondary into the disk in the counter-rotating solar metallicity model (hereafter, the SR-model) is more energetic than in the co-rotating models, because the relative velocity of the encounter is higher. However, we observe a lower median gas temperature in the SR-model relative to the S-model. This apparent discrepancy can be explained by the fact that the counter-rotating gas disk efficiently shears the shock formed by the impact of the secondary black hole. The hot gas from the shock front is quickly

transported away from the secondary and its thermal energy is radiated. When compared to each other, the three models exhibit an interesting property: while the *median* gas temperature is 3×10^5 , 5×10^5 , and 10^6 K, the *mean* temperature is 10^{11} , 10^{10} , and 10^9 K, in the SR, S, and BB-models respectively.

Another property of the SR-model is that its cooling curve does not exhibit peaks at the times of the pericentric passages of the binary (Figure 13). The peaks noticeable in the cooling curve occur, respectively, one and two years after the pericentric passages and are not associated with the peaks in the accretion rate (Figure 14). This implies that along with accretion there must be an additional mechanism that powers the bolometric emission. This second heating mechanism, which competes with photoionization, arises from shocks in the gas. The bolometric luminosity of the gas disk settles at $\sim 10^{45} \text{ erg s}^{-1}$ and the luminosity of the photoionization

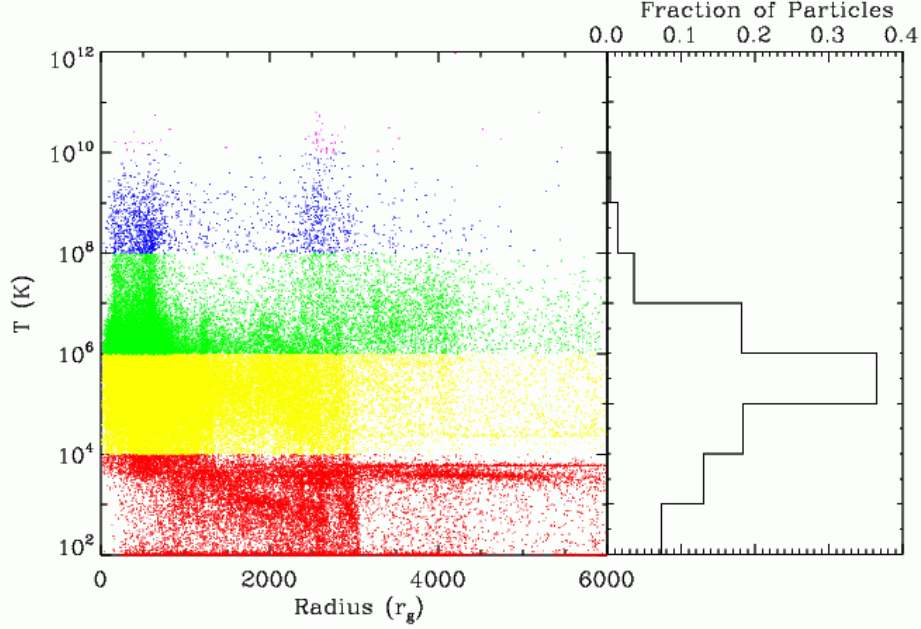


FIG. 8.— *Left*: Temperature of gas cells as a function in the disk which was partially hidden in the xy -projection in Figure 7. The colors that mark each temperature band are used throughout the paper. This figure corresponds to the morphology of the disk plotted in panel 2 of Figure 7. *Right*: Histogram showing the fraction of particles as a function of temperature.

sources is $\sim 10^{44} \text{ erg s}^{-1}$.

In the counter-rotating model, the gas is driven away from the center of the disk, as it acquires more orbital angular momentum from the binary, and the hollow region around the primary widens with time. This is why during a pericentric passage there is no characteristic jump in the accretion rate of the primary, and accretion occurs by smooth diffusion of particles from the disk. However, the accretion rate onto the secondary shows peaks corresponding to pericentric passages, and smooth undulation in between. Although over the course of the two orbits we do not notice a decrease in the accretion rate, if the outbound migration of gas continues and the low density gap is formed at the center, the accretion on the primary is likely to dwindle. Observationally, this implies that in these systems, only one of the sources (the secondary)

may remain active, until its orbit gradually becomes smaller than the hollow region in the disk, at which point both black holes may stop accreting. Whether both, one, or neither of the two sources are seen in emission depends on the evolutionary stage of the binary and the thermodynamic properties and supply of the low angular momentum gas in the host galaxy.

A noticeable feature in the accretion curve of the primary is a dip between the 8th and 12th years. This corresponds to the time when a large portion of the gas is unbound from the disk, as shown in the second panel of Figure 11. The detached part of the disk continues to revolve around the primary until it is re-captured and wound around. After it has completed several orbits, this gas creates a complex set of rings and filaments. A

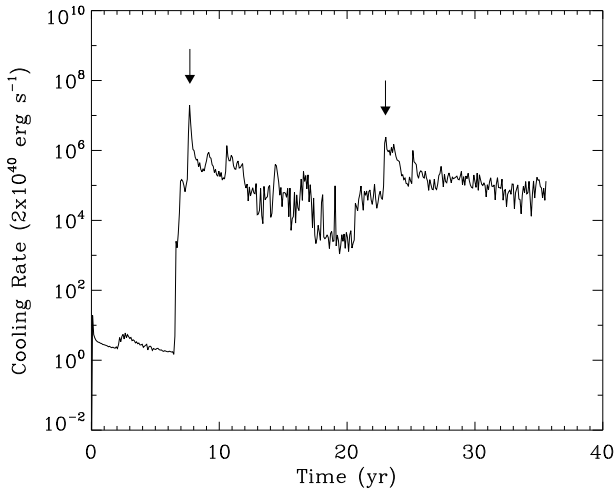


FIG. 9.— Cooling rate of the gas as a function of time calculated from the S-model. The cooling rate shown here traces the bolometric light curve of the gas disk. The arrows mark the times of pericentric passages of the binary.

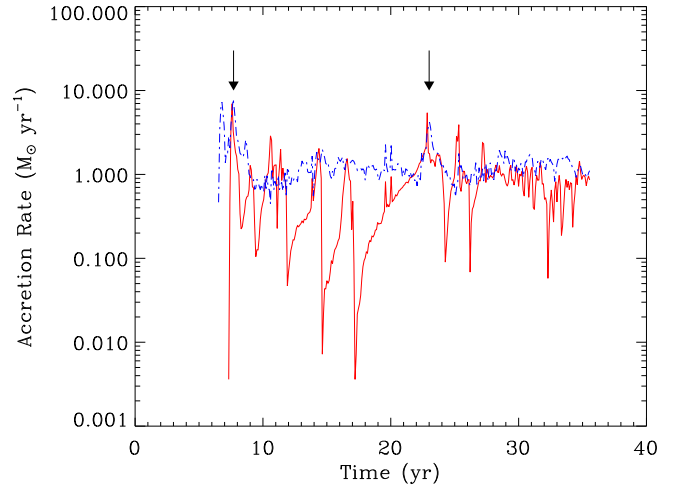


FIG. 10.— Effective accretion rate on the primary (solid, red line) and secondary (dashed, blue line) black holes calculated from the S-model. The accretion rate curves can be translated into UV/X-ray light curves by assuming that $1 M_{\odot} \text{ yr}^{-1} \sim 10^{43} \text{ erg s}^{-1}$ of UV/X-ray luminosity. The arrows mark the times of pericentric passages of the binary.

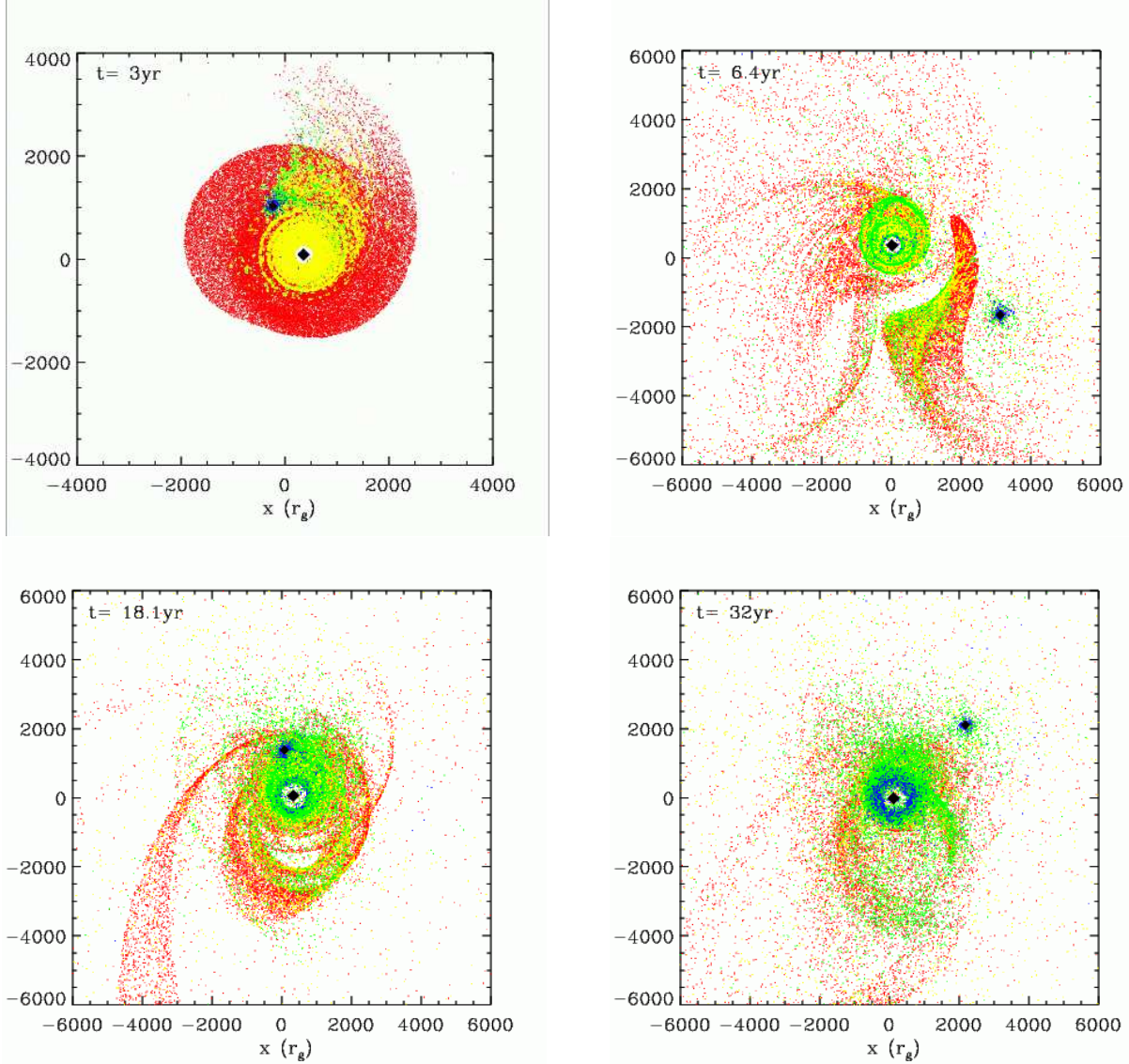


FIG. 11.— Sequence of snapshots from the simulation showing the evolution of the binary and gas in the SR-model (projected into the plane of the binary orbit). The time stamp is marked on the top of each panel. The first snapshot shows the system shortly after the secondary plunges into the disk for the first time. The rotation of the binary is counter-clockwise and that of the disk is clockwise. Note that higher temperature particles are plotted over the lower temperature ones, with the result that some information is hidden (also see Figure 12).

fraction of this gas will fall into the primary black hole and boost its accretion rate back to $\sim 1 M_{\odot} \text{ yr}^{-1}$.

3.4. X-ray Light Curves

We calculate the X-ray luminosity powered by the two different mechanisms: accretion and bremsstrahlung emission from the hot gas. The bremsstrahlung emitting gas is heated by both, shocks and photoionization. The accretion rates onto the primary and secondary black holes estimated from the S and SR-models result in a UV/X-ray luminosity of about $10^{43} \text{ erg s}^{-1}$ and up to $10^{44} \text{ erg s}^{-1}$ during times of high accretion rate (the details of the accretion curves in each model are discussed in § 3.2 and § 3.3 and shown Figures 10 and 14).

In this section we describe how the estimate of the concurrent bremsstrahlung X-ray luminosity was obtained. We calculate the thermal bremsstrahlung power per unit volume from the population of relativistic electrons hotter than 10^7 K

as

$$\Lambda_{\text{brems}} = 1.4 \times 10^{-27} T^{1/2} Z^2 n_e n_i \times \overline{g_b} (1 + 4.4 \times 10^{-10} T) \text{ erg cm}^{-3} \text{ s}^{-1}, \quad (18)$$

where Z is the atomic number, n_e and n_i are the number densities of electrons and ions, respectively, $\overline{g_b}$ is a frequency average of the velocity averaged Gaunt factor and is of order 1. The electrons are heated in the process of photoionization of the gas by the accretion powered sources and in shocks taking place in the gas perturbed by the secondary black hole. In order to calculate the resulting bremsstrahlung X-ray luminosity, we also need to know the volume occupied by the gas giving rise to this emission. The calculation of the size of the emitting volume from a SPH simulation is complicated by the finite spatial resolution, as set by the characteristic size assigned to each gas particle (i.e., the smoothing length, h_{sml}). In our calculations $h_{\text{sml}} \geq 10 r_g \approx 10^{14} \text{ cm}$. As a result of “smoothing”, the bremsstrahlung X-ray emis-

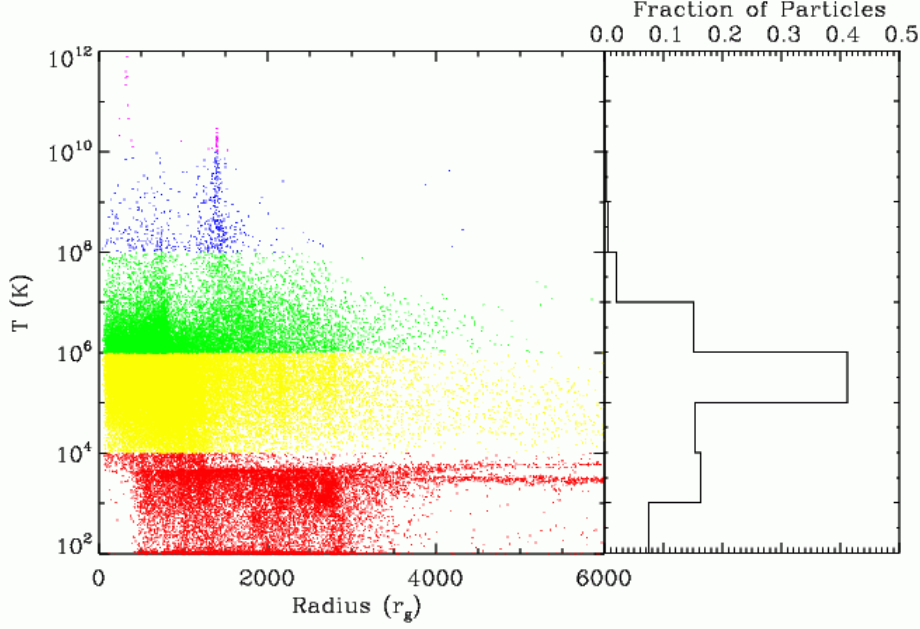


FIG. 12.— *Left*: Temperature of gas cells as a function of radius at 18.1 years in SR-model. This figure shows the extent of temperature stratification in the disk which was partially hidden in the xy -projection in Figure 11. The colors that mark each temperature band are used throughout the paper. This figure corresponds to the morphology of the disk plotted in panel 3 of Figure 11. *Right*: Histogram showing the fraction of particles as a function of temperature.

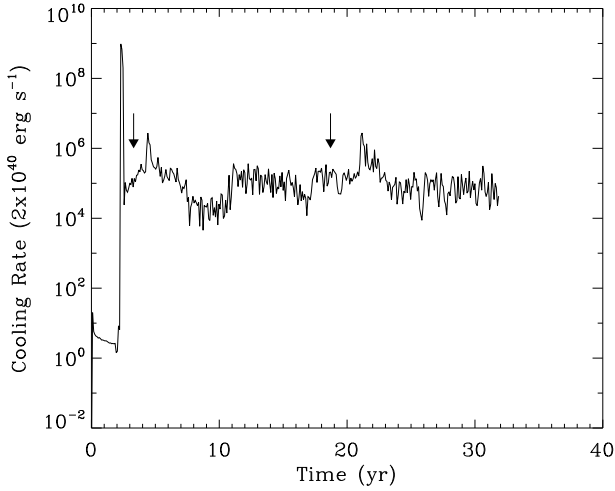


FIG. 13.— Cooling rate of the gas as a function of time calculated from the SR-model. The cooling rate shown here traces the bolometric light curve of the gas disk. The arrows mark the times of pericentric passages of the binary.

sion from shocks, which typically occur on scales smaller than h_{sml} in our simulations, is not resolved. Consequently, the size of the emission region in this case is overestimated, while the density and the temperature in the shock are underestimated. In order to bypass this uncertainty we calculate the values of some physical properties of the X-ray emitting gas following the analytical treatment of shock structure in Hollenbach & McKee (1979).

First, we attempt to discriminate between the gas particles in the photoionized and shocked regions. We assume that gas particles that have a Mach number $\mathcal{M} > 10$ can participate in shocks and thus contribute to the *shock-powered* bremsstrahlung X-ray emission. From the jump conditions we calculate the compression and temperature ratios in the

shocked gas cell and from these we estimate the post-shock density and temperature of the gas. Using the post-shock values of the physical parameters we calculate the cooling rate (equation [18]) and cooling time for the shocked gas cell under the assumption that its dominant cooling mechanism is bremsstrahlung. The corresponding cooling column of gas is then $N_{cool} = n_0 v_s t_{cool}$, where n_0 is the pre-shock density of the gas, v_s is the velocity of the shock, and t_{cool} is the cooling time. The values of the cooling column and the post-shock density of the hot gas allow us to estimate the characteristic length scale of the cooling column, ℓ_{cool} . For typical values of the parameters in the shocked gas cells in our simulations, where $n_e \approx n_i \approx n \sim 10^{12} - 10^{13} \text{ cm}^{-3}$ and $T \sim 10^8 \text{ K}$, we obtain $\ell_{cool} \sim 10^9 \text{ cm}$. We use this information to constrain the X-ray emitting volume within a shocked gas cell. Given that 60–70% of gas particles fulfill the condition $\mathcal{M} > 10$ and post-shock $T > 10^7 \text{ K}$, we find that the resulting bremsstrahlung X-ray luminosity from the shocked gas is in the range $10^{40} - 10^{42} \text{ erg s}^{-1}$, with peaks reaching $10^{43} \text{ erg s}^{-1}$.

In the second step we estimate the bremsstrahlung X-ray luminosity emitted from the photoionized portion of the gas. We identify the gas cells responsible for most of the X-ray emission *powered by photoionization* as low density cells with temperatures higher than $T > 10^7 \text{ K}$. The hot, optically thin, photoionized component of the gas forms a halo with a median density of $n \sim 10^7 - 10^8 \text{ cm}^{-3}$. The photoionized regions are more spatially extended than the shocked regions and their characteristic scale is $\ell_{cool} \sim 10^3 r_g \approx 10^{16} \text{ cm}$. The number of photoionized gas particles that contribute to the X-ray bremsstrahlung emission at any given time is about a few percent of all gas particles. However, the large volume of this halo makes up for its small mass and low number density. Thus, the resulting bremsstrahlung luminosity from the halo is $10^{41} - 10^{42} \text{ erg s}^{-1}$, comparable to the estimated contribution of the shocked regions.

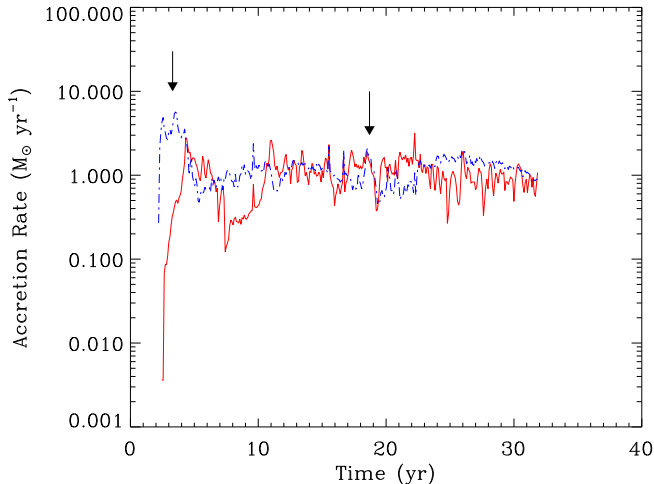


FIG. 14.— Effective accretion rate on the primary (solid, red line) and secondary (dashed, blue line) black holes calculated from the SR-model. The accretion rate curves in our calculations can be translated into UV/X-ray light curves from the emission sources, where $1 \text{ M}_\odot \text{ yr}^{-1} \sim 10^{43} \text{ erg s}^{-1}$ of UV/X-ray luminosity. The arrows mark the times of pericentric passages of the binary.

We emphasize that the estimates of the bremsstrahlung X-ray luminosity presented here are based on astrophysically motivated but simplified assumptions. For example, while $\mathcal{M} > 10$ may be a necessary condition for a gas particle to participate in shocks, not every such particle will do so. The shocks may be avoided in ordered, laminar flows where the trajectories of particles do not intersect. However, we expect that the gravitational perturbation from the secondary black hole will cause shocks, especially in the inner portion of the disk where the dynamical time scale of particles is much shorter than the period of the binary and the density of the gas is higher. In the case of photoionization, not all hot, low density gas particles will be entirely photoionized, making the effective emitting volume (or equivalently the emitting mass) only a fraction of the total in a gas cell. There may also be particles which participate in shocks and are at the same time photoionized by the accretion powered sources. For all these reasons and because the structure of the nuclear region is very complex, we note that the above estimates should be regarded as constraints rather than exact values.

The total bremsstrahlung X-ray luminosity (shock plus photoionization powered) of the gas in our simulations is lower than the accretion-powered UV/X-ray luminosity, although during the times of pericentric passage the peak bremsstrahlung X-ray luminosity is comparable to the accretion-powered X-ray luminosity. The latter X-ray light curve exhibits peaks during pericentric passages of the binary, thus the peaks are good markers of such events. The estimated level of the total X-ray emission (accretion powered plus bremsstrahlung) should be observable to a redshift of $z \lesssim 2$ during the outburst phases.

Although our calculations follow the evolution of the binary over only two orbital passages we suggest that in binary systems of this type, X-ray outbursts should be expected to continue as long as there is gas in the nuclear region for the binary to interact with. Our models imply that at the mean level of accretion, the gaseous disks should be depleted after $10^3 - 10^4 \text{ yr}$. In order for the outburst activity to last for longer time scales, the reservoir of gas in the nuclear region needs to

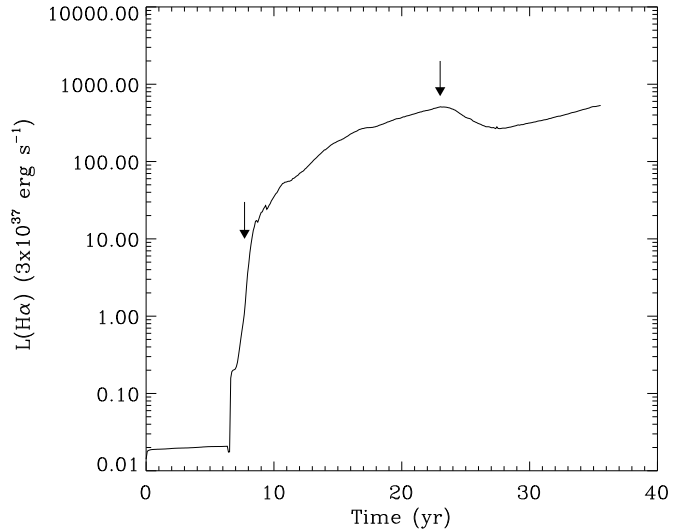


FIG. 15.— $H\alpha$ light curve for the S-model obtained with help of photoionization calculations. The arrows mark the times of pericentric passages of the binary. The details of the method are described in § 2.3 of the text.

be continually replenished. It is also plausible, however, that repeated collisions of the secondary black hole with the disk will completely disrupt it and turn it into a spherical halo of hot gas. In such a case, the accretion rate would be relatively smooth and uniform, and no outburst would be evident.

A calculation following the X-ray light curve variability over a large number of orbits is necessary in order to confirm that the periodicity is a long lived signature of the binary. Although currently not possible with the SPH method used here, simulations of the long term evolution of the binary together with hydrodynamics and radiative transfer may be achieved in the future by a hybrid approach including complementary numerical techniques. In particular, they may be realized by combining semi-analytical hydrodynamical calculations with emphasis on the long term dynamical evolution of gas with methods that focus on hydrodynamics and radiative transfer, like the one used here.

3.5. $H\alpha$ Light Curves and Broad Emission Line Profiles

By modeling the $H\alpha$ light curves for the S and SR-models we find that after the beginning of accretion the $H\alpha$ luminosity gradually reaches $10^{39} - 10^{40} \text{ erg s}^{-1}$ in both models (Figures 15 and 16). Sources with such $H\alpha$ luminosities are observable out to the distance of the Virgo Cluster and possibly up to a distance of 100 Mpc. During the steady-state phase, before the plunge of the secondary into the disk, both models are characterized by a low $H\alpha$ luminosity, $L_{H\alpha} \sim 10^{35} \text{ erg s}^{-1}$. This is an artifact of the calculation, a consequence of the choice of initial conditions, because in the pre-plunge phase the emission from the gas is entirely thermal emission from the disk and the effects of photoionization are not taken into account. Such neutral and non-illuminated accretion disks are unlikely to be encountered in nuclear regions of AGNs, even if these are characterized with very low accretion rates.

Although in our model the $H\alpha$ light is closely linked with accretion, it does not closely follow the variations in the accretion rate. Neither the $H\alpha$ light curve exhibits easily recognizable periodic features during the first two orbits of the binary. The only occasion when a noticeable jump in the $H\alpha$ luminosity occurs is in the SR-model, after the first pericen-

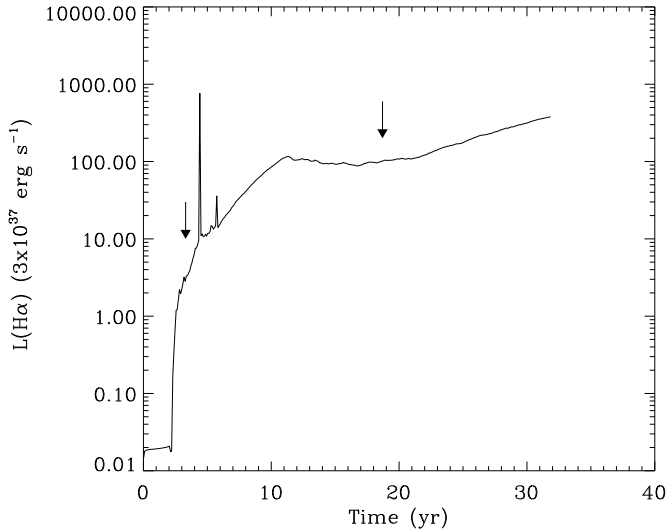


FIG. 16.— $H\alpha$ light curve obtained with help of photoionization calculations used in the SR-model. The first, large spike in the light curve occurs after the first pericentric passage of the binary (the arrows mark the times of pericentric passages). The details of the method are described in § 2.3 of the text.

tric passage (Figure 16). The $H\alpha$ light is predominantly contributed by a spatially extended component of the gas and is less susceptible to shocks by the secondary. The gradual increase in the $H\alpha$ luminosity noticeable in both light curves is caused by the redistribution of the photoionized gas in space. As gas expands to a scale of a parsec, its density and optical depth decrease, and the solid angle subtended to the photoionizing source increases. As a result, a larger fraction of ionizing photons is reprocessed to $H\alpha$ photons and the physical properties of the gas evolve towards those found in photoionized nebulae.

It appears difficult to infer the existence of a binary in the nuclear region of a galaxy based on the $H\alpha$ light curve alone. Serendipitous flares in the $H\alpha$ light curve may occur close to pericentric passages but their duration may be fairly short (here, \leq month, the upper limit set by the time resolution in the light curve) and consequently hard to observe. The periodic outbursts may be more pronounced in cases when the binary orbit is inclined with respect to the disk, but such models remain to be explored.

We also calculate the broad $H\alpha$ emission-line profiles for both the S and SR-models in order to better illustrate the kinematics of the gas (see Figures 17 and 18). All profiles have been calculated under the assumption that the observer is located at a distance $d \rightarrow \infty$ in the positive xz -plane, at $i = 30^\circ$ to the z -axis. Initially, from the unperturbed disk we observe double-peaked emission line profiles but they gradually depart from this shape as the perturbation propagates through the gas. For reasons discussed above, the regular $H\alpha$ profiles from a quiescent, cold disk, have a low intensity. The profiles appear variable on a time scale of months to years, both in shape and width. The profiles in both sets show an extended, low intensity red wing, most pronounced during the periods of increased accretion and after the times of pericentric passages. During such events a number of emitting gas particles find themselves deeper in the potential well of the binary. The emitted photons that leave the potential well are gravitationally redshifted and Doppler boosted, thus con-

tributing to the extended red wing and the blue shoulder of the relativistic $H\alpha$ profiles. The changes in the profile sequence can be better seen in the trailed spectrograms, shown in Figures 19 and 20, which are the 2D maps of the $H\alpha$ intensity against observed velocity (or wavelength). The $H\alpha$ emission in the trailed spectrograms from both S and SR-models appears redshifted relative to the rest wavelength. In addition, the emission in the extended red wing of the profile is easily noticeable, especially in the SR-model (Figure 20), where this effect is most dramatic after the pericentric passages of the binary. Since Doppler boosting of the blue side of the line and gravitational redshift of the red wing are pronounced during and after the pericentric passages of the binary, they can serve as indicators of the orbital period. In the trailed spectrogram of the S-model it is possible to discern the repeating behavior in the windows between 7 to 22 years and 22 to 36 years. The width of the $H\alpha$ profile increases after the pericentric passages of the system, reflecting the inflow of gas towards the primary. Additionally the widening of the profile appears asymmetric and shifted towards the red with respect to the pre-pericentric sequence of profiles. This shift is a signature of the motion of the accretion disk which follows the primary on its orbit. The shift is even more pronounced in the trailed spectrogram of the SR-model which also exhibits narrower emission line profiles than the S-model. This difference arises from the difference in kinematics of the innermost portion of the accretion disk surrounding the primary. In the SR-model the gas at the inner edge of the disk becomes gradually less bound to the primary black hole over time due to the interactions with the binary. We compare the trailed spectrograms with the velocity curves of the two binary components projected onto the line of sight (right panels in Figures 19 and 20). Because of the nonzero eccentricity of the orbit the velocity curves appear skewed. The variations in the profile intensities in the S-model correspond to the features in the velocity curve of the secondary in year 7 and 23, when it moves away from the observer with the highest projected velocity. In the SR-model the velocity curve of the secondary appears as a mirror image of certain features in the trailed spectrogram because in this model the gas rotates in the opposite direction with respect to the binary. In general, we expect the signature of the velocity curves of the two black holes to appear in the emission line profiles at pericentric passages, because that is when the binary interaction with the gas is strongest. If such features could be discerned in the observed $H\alpha$ emission-line profiles, they would signal the presence of a binary.

In practice, one may constrain the period and the mass ratio of the binary from the periodicity and projected velocity components of the two black holes, all measured from the $H\alpha$ profile sequence. The determination of the individual black hole masses is more challenging, because it requires knowledge of the inclination of the binary orbit with respect to the observer. In general, the inclination of the binary orbit may not be the same as that of the accretion disk but in some cases it may be possible to determine it relative to the accretion disk. If the binary orbit is *circular*, fewer parameters are needed to constrain the properties of the system, and it should be possible to determine the individual masses of black holes, given a knowledge of the observed velocity components of the two black holes at a single point of time, orbital period, and the inclination of the system. To constrain the shape and the orientation of an *elliptical* binary orbit one would in addition need information about the velocity components at pericenter and apocenter, as well as the orbital separation of the bi-

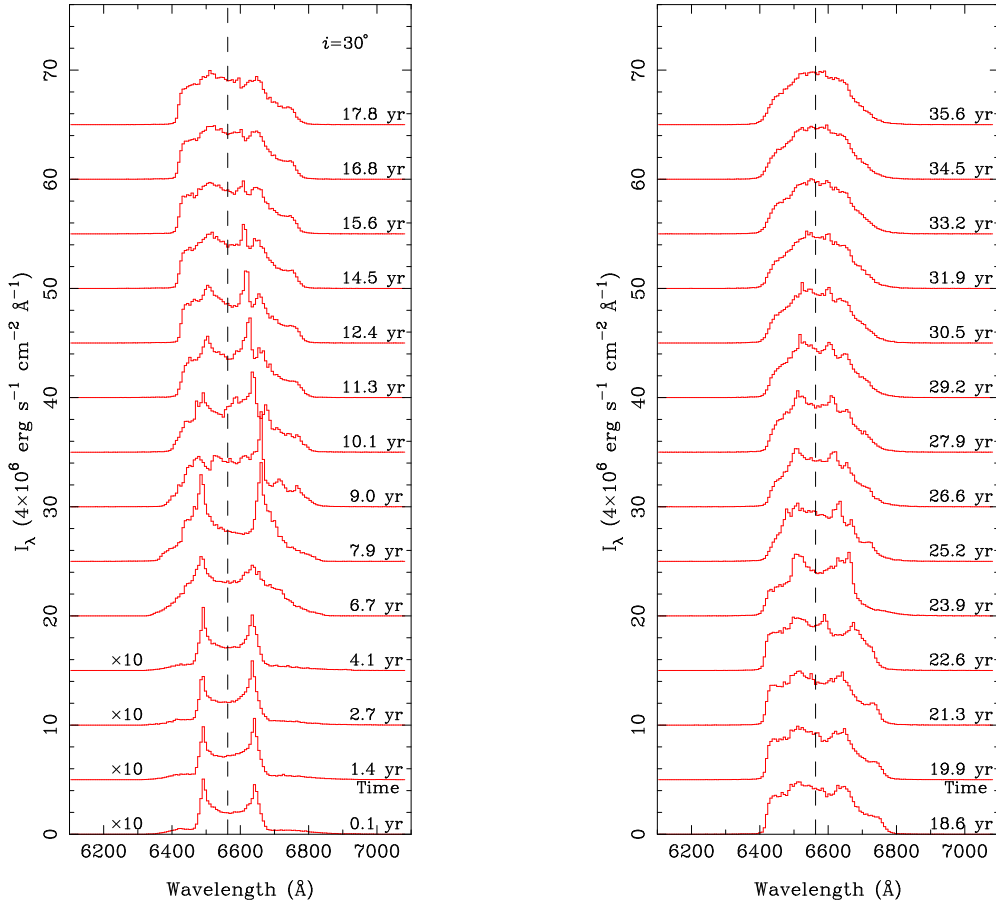


FIG. 17.— Sequence of the H α emission-line profiles selected from the S-model. The intrinsic intensity of profiles is plotted against wavelength. The first 4 profiles in the sequence are multiplied by a factor of 10, so that they can be represented on the same intensity scale with the other profiles. The corresponding time from the beginning of the simulation is plotted next to each profile. The inclination of the plane of the disk with respect to the observer is as marked on the figure. The vertical dashed line at 6563 Å marks the H α rest frame wavelength.

nary. Before any of these parameters can be measured from observations of light curves and the H α line sequence, it is necessary to follow at least a few revolutions of the binary.

We note several other qualitative features of the H α profiles, which can shed light on the motion of gas in the nuclear region. In both models, the central part of the profile, contributed by emission from the low velocity gas, becomes more pronounced with time. This low velocity core of the profile is contributed by filaments of gas which have been expelled from the center at the expense of the angular momentum of the binary. The same effect re-appears during the second orbital passage when a new low velocity component is added to the system. In this process filaments with a similar morphology are formed during each passage, on a slightly different length scale, because the older filaments have had time to expand, and with a slightly different phase, due to the effect of rotation.

Although it is expected that all AGNs host black holes fed by an accretion disk, broad, double or multi-peaked emission-line profiles are observed only in a small fraction of objects (Eracleous & Halpern 2003; Strateva et al. 2003). The appearance of the H α line profiles can be affected by physical conditions in the nuclear region, other than the phase-space distribution of the emitting gas, such as optical depth to H α photons and electron scattering. Figure 1 illustrates that a significant fraction of the H α light is contributed by the hot ionized gas located in the inner disk, via recombination. This

component of the gas is transparent to H α photons (Figure 2). Nevertheless, the profiles will likely be affected by the high H α opacity in regions of the disk where the gas temperatures are just below $\sim 10^6$ K and the neutral hydrogen column density is high (Figure 21).

The second factor, which impacts the shape of the H α emission-line profile, but to a lesser extent the H α luminosity, is electron scattering. As expected, the ionized gas will have the highest optical depth to Thomson scattering (Figure 22). We find that the maximum value of τ_T in our calculation is about 10, observed for the hottest gas cells. About 60% of the mass of the gas has optical depth to Thomson scattering larger than 1, in our simulations. When Thomson scattering is significant, the hot corona with a high thermal velocity dispersion ($c_s \sim 10^2 - 10^3$ km s $^{-1}$) could smooth out some emission features in the H α profiles, although the emission profiles should still show up clearly. Such conditions can be met in nuclear regions hosting a strong photoionization source.

Although the effects of optical depth in the gas can play an important role in estimates of H α luminosity and appearance of the H α emission line profiles, we are not able to account for these effects in our calculations. We used conservative values for the model parameters, such as the radiative efficiency and covering factor, throughout the paper so that the H α luminosity is not significantly over-estimated. The problem of the propagation of photons along the line of sight is numerically complex and is likely to be accurately treated with the new

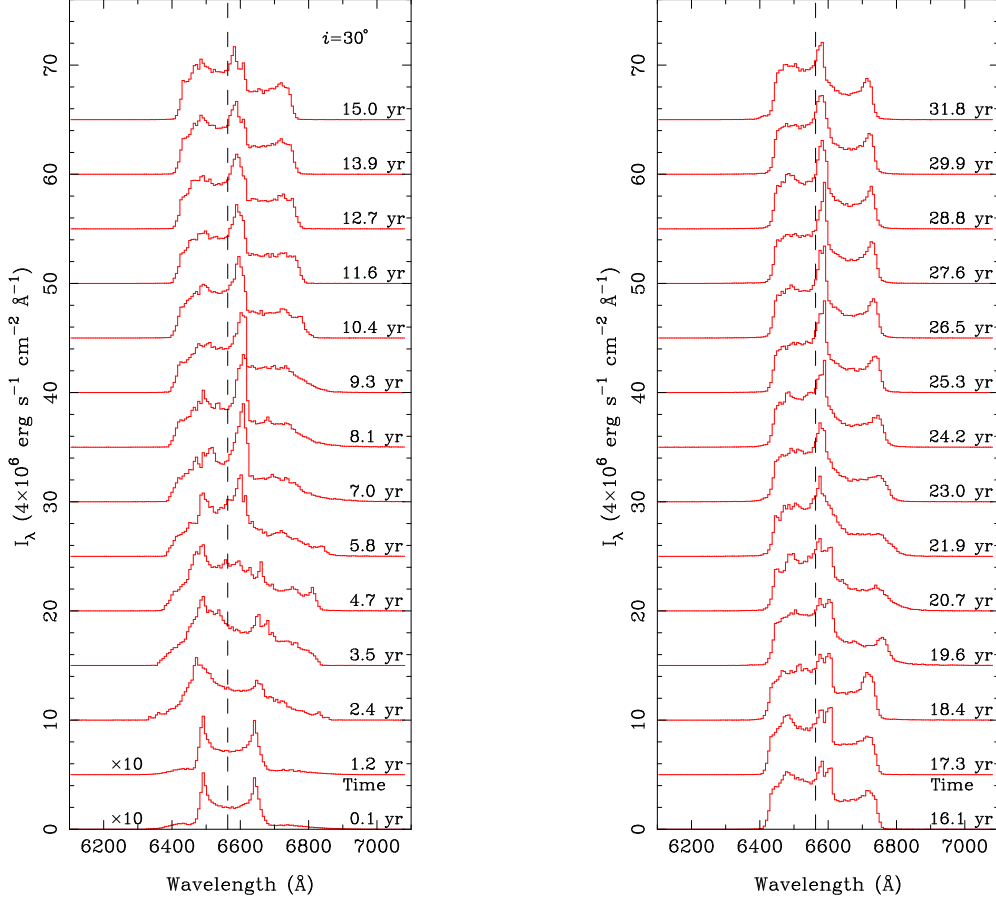


FIG. 18.— Same as previous figure, except for the SR-model. The first 2 profiles in the sequence are multiplied by a factor of 10, so that they can be represented on the same intensity scale with the other profiles.

generation of codes which incorporate ray-tracing techniques in the radiative transfer calculations.

3.6. Evolution of the Binary Orbit

In this section we describe the changes in the binary orbit due to interactions with the gas and compare them with analytical estimates. The evolution of the binding energy and orbital angular momentum of the binary in the BB, S, and SR-model is shown in Figures 23, 24, and 25, respectively. In all three models the binary system shows a net loss of both energy and orbital angular momentum. The mean dissipation rate of the binding energy, calculated from the simulations is $dE/dt \approx 4 \times 10^{46} \text{ erg s}^{-1}$ for the BB-model and $1 \times 10^{46} \text{ erg s}^{-1}$ in the S, and SR-model. As a result the second pericentric passage in the S-model occurs about 100 days later than in the BB-model (see Figures 4 and 7 at a time of 23.2 years). The mean rate of energy dissipation due to emission of gravitational radiation is $(dE/dt)_{\text{gw}} \approx 7 \times 10^{42} \text{ erg s}^{-1}$ and thus the evolution of the binary orbit is dominated by interactions with the gas. Because the rate of gravitational wave emission is very similar for all three models we show it only once, in the inset of Figure 24.

In all three models the binary is initially placed on the same orbit, hence the differences in evolution of the orbital parameters among the models are entirely due to the kinematic and thermodynamic properties of the gas. Recall that in the BB-model the gas initially redistributes into two phases with a temperature contrast of about an order of magnitude (§ 3.1). The cold phase present in the BB-model is missing in the

S-model, where the secondary black hole interacts with the warmer and more tenuous gas and consequently dissipates its energy more gradually. This is consistent with the findings of Escala et al. (2005) that the binary evolution depends strongly on the “clumpiness” of the gas, and that the binary suffers a stronger deceleration in gaseous media with weaker pressure support. After the first pericentric passage, the cold gas phase in the BB-model disappears, due to shock and photoionization heating, and E and L evolve in a less dramatic way.

The rates of dissipation of energy and orbital angular momentum in Figures 23, 24, and 25 are functions of the orbital phase of the binary because the binary spends a fraction of its time moving through the disk. Therefore, the interaction of the binary and the accretion disk occur in two different regimes studied by Lin & Papaloizou (1979a,b). In the first regime the disk is confined to the Roche lobe of the primary black hole and the secondary is outside the disk and interacts with it tidally. For a mass ratio q and a Reynolds number \mathcal{R} Lin & Papaloizou (1979a) show that when $q > \mathcal{R}^{-1}$, the tidal force overtakes the viscous expansion of the disk, and the secondary effectively removes the angular momentum at the outer edge of the disk by truncating the disk (in our simulations $q = 0.1$ and $\mathcal{R} \sim 10^5$). The excess angular momentum is transported to the binary via tidal torques. In the second regime, the secondary is orbiting within the circumbinary disk and truncate the inner edge of the disk (Lin & Papaloizou 1979b) through its tidal forces. In this regime the disk acts as an effective energy and angular momentum sink and the binary should evolve towards a more bound state via resonant

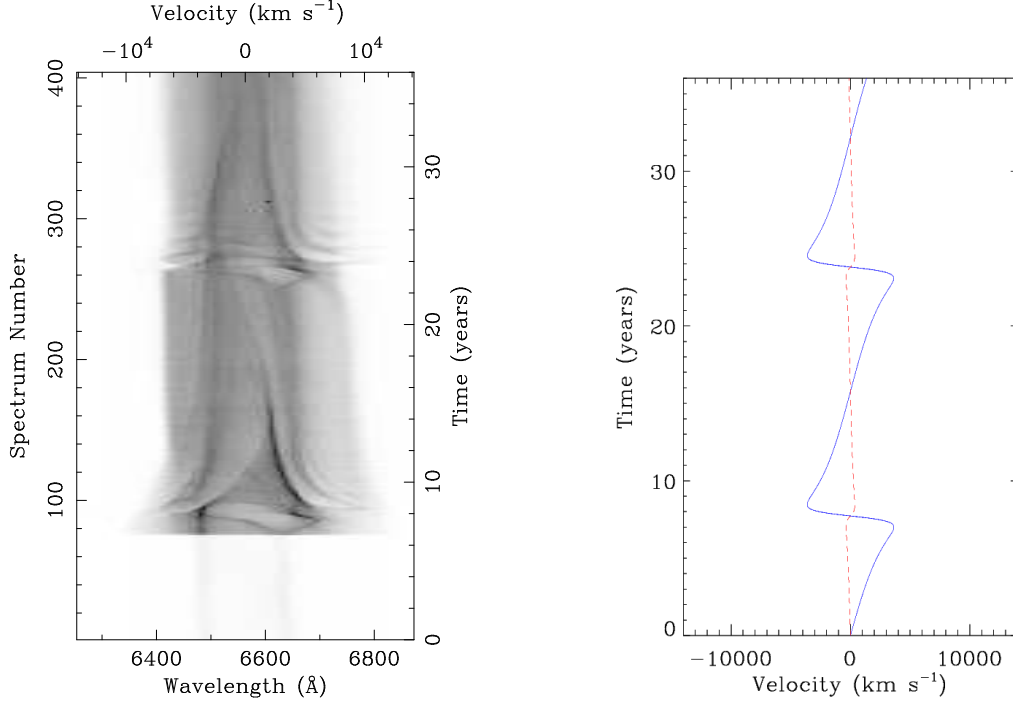


FIG. 19.— Trained spectrogram (left) and black hole velocity curves (right) plotted for the S-model. The trained spectrogram is a logarithmic gray scale map of the H α intensity against wavelength and observed velocity. Darker shades mark higher intensity. Notice the low relative intensity of profiles before the start of accretion. The velocity curve panel shows the orbital velocities of the primary (*dashed, red line*) and secondary (*solid, blue line*) black holes projected along the line of sight to the observer. The velocity curves are skewed because of the non-zero eccentricity of the orbit.

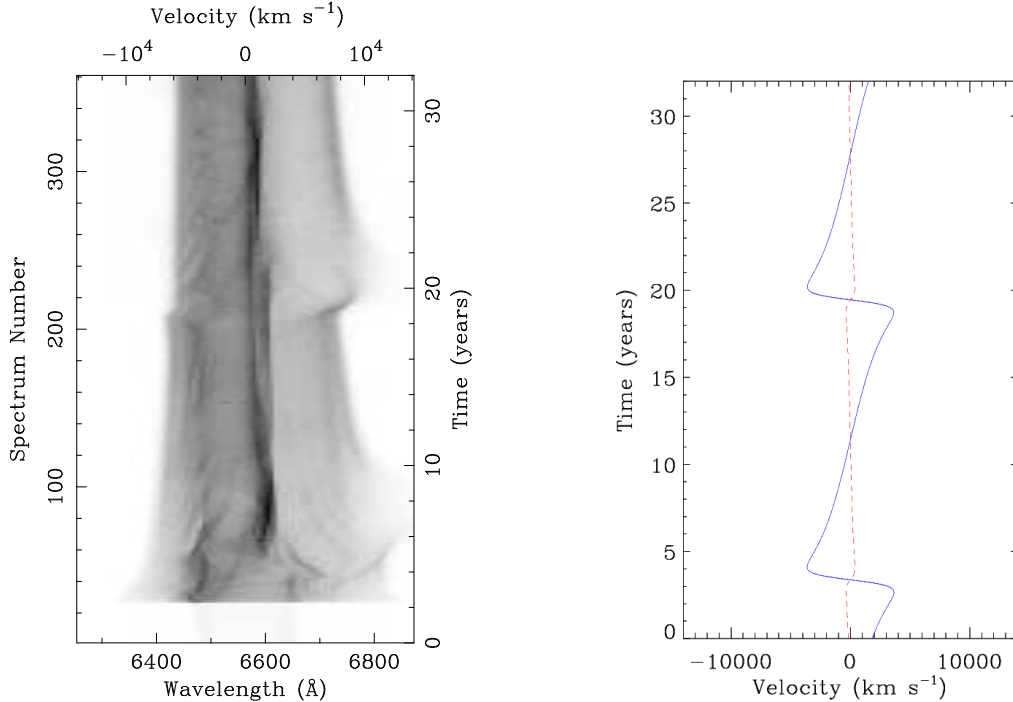


FIG. 20.— Trained spectrogram (left) and black hole velocity curves (right) plotted for the SR-model. The trained spectrogram is a logarithmic gray scale map of the H α intensity against wavelength and observed velocity. Darker shades mark higher intensity. Notice the low relative intensity of profiles before the start of accretion. The velocity curve panel shows the orbital velocities of the primary (*dashed, red line*) and secondary (*solid, blue line*) black holes projected along the line of sight to the observer. The velocity curves are skewed because of the non-zero eccentricity of the orbit.

interactions with the disk. This is qualitatively consistent with our findings from the BB and S-models, where the binary is co-rotating with the disk and is found to reach the minimum binding energy when both black holes are close to the pericenter and within the disk.

An additional torque arises from the fact that the velocity vectors of the binary on the elliptical orbit and the gas around the primary on circular orbits continuously change their respective orientation; thus the torque acting on the binary changes accordingly. In the co-rotating case, the sec-

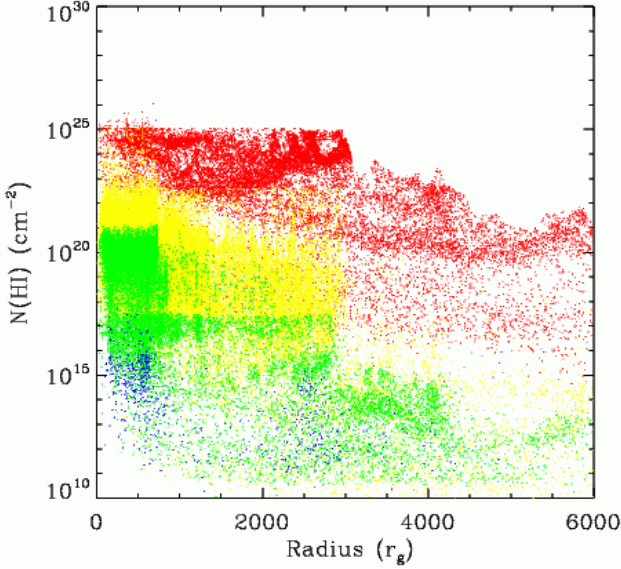


FIG. 21.— Neutral hydrogen column density of the gas as a function of radius, at a time of 9.4 years in the S-model. The colors mark the temperatures of gas particles and are the same as in earlier figures. This figure corresponds to the morphology of the disk as plotted in panel 2 of Figure 7.

ondary experiences a torque that pushes it away from the primary as it approaches pericenter and a torque that pushes it inwards as after it passes pericenter. This effect can be seen in Figure 24: the binary evolves from a more bound to a less bound energy state as it passes pericenter and the slope of the energy curve is negative. In the counter-rotating case, the secondary and the disk orbit in the opposite sense and the effect of torques is reversed. Figure 25 shows this reversal: the slope of the energy curve is positive during the pericentric passage.

We first compare the rate of dissipation of orbital energy of the binary with that predicted by Ostriker (1999) for the case where a massive perturber moving supersonically experiences the dynamical friction force arising from the wake that formed in the ambient medium. This rate can be expressed as

$$\left(\frac{dE}{dt}\right)_{df} = \frac{4\pi(GM_p)^2\rho}{v} \ln\left(\frac{r_{max}}{r_{min}}\right) \approx 2 \times 10^{46} \left(\frac{M_p}{10^7 M_\odot}\right)^2 \left(\frac{n}{10^{11} \text{ cm}^{-3}}\right) \left(\frac{v}{10^4 \text{ km s}^{-1}}\right)^{-1} \text{ erg s}^{-1}, \quad (19)$$

where M_p and v are the mass and velocity of the perturber, ρ is the density of the gaseous medium, and r_{max} and r_{min} are related to the linear size of the medium and the perturber. If we assume that r_{max} is comparable to the radius of the disk and r_{min} to the accretion radius of the black hole, then $\ln(r_{max}/r_{min}) \approx 5$. In our simulations the wake of the hot gas trailing the secondary black hole can be seen in panel 1 of Figures 4 and 7.

However, as discussed by Lin & Papaloizou (1979a,b), tidal torques and resonant scattering play an important role in the interaction of a binary with a shear flow. We also note that dynamical friction cannot be the dominant dissipation mechanism in the SR-model. In this model, the disk rotates in the opposite sense from the binary and the wake formed by the secondary is efficiently sheared away from the secondary. We

utilize the expression from Lin & Papaloizou (1979b) for the tidal torque exerted by the binary on the disk in the process of gap formation and obtain

$$\left(\frac{dE}{dt}\right)_t = \frac{8}{27} q^2 \Omega^3 r^4 \Sigma \left(\frac{r}{A}\right)^3 \approx 6 \times 10^{45} \left(\frac{q}{0.1}\right)^2 \left(\frac{M_p}{10^7 M_\odot}\right)^{3/2} \left(\frac{n}{10^{11} \text{ cm}^{-3}}\right) \left(\frac{H}{50 r_g}\right) \times \left(\frac{r}{10^3 r_g}\right)^{5/2} \left(\frac{A}{10^2 r_g}\right)^{-3} \text{ erg s}^{-1} \quad (20)$$

where Ω is the angular velocity of the gas interacting with the black hole at radius r , Σ is the surface density of the gas disk, A is the half-size of the gap, and H is the half-thickness of the disk. The results of our simulations are consistent with both mechanisms being responsible for the dissipation of the binary orbital energy. We also note that dynamical friction cannot be the dominant dissipation mechanism in the case of the binary and gas disk rotating in the opposite sense from each other. Assuming that the binary maintains a rate of energy dissipation of $\sim 10^{46} \text{ erg s}^{-1}$, it would proceed to coalescence in only $\sim 10^3 \text{ yr}$. Most likely, the rate of inspiral due to interactions with the gaseous background will not persist at this high rate over long periods of time. Armitage & Natarajan (2002) for example discussed the evolution of a binary on a circular orbit, in the gas disk, from separations of 0.1 to 10^{-3} pc . Extrapolating from their results one obtains that from the separation of 0.01 pc, a combination of disk-driven migration and inspiral due to gravitational radiation leads to coalescence within $\text{few} \times 10^6 \text{ years}$. In order to obtain a robust estimate of the orbital decay rate one should follow the evolution of the binary and gas starting from much larger separations. While this task was undertaken by a number of authors (Kazantzidis et al. 2005; Escala et al. 2004, 2005; Dotti et al. 2006a; Mayer et al. 2006a) it is still a computational challenge to extend the wide dynamic range of the simulations to the lowest binary separations, where gravitational radiation overtakes the dissipation caused by the gaseous background.

4. DISCUSSION

Here we discuss the impact of underlying assumptions in our models on the observable electromagnetic signatures and the relevance of our results in the context of the larger scale simulations.

Mass of the gas disk. A more massive disk would change the gas drag, hence make the binary evolve faster and vice versa. This would affect the number of pericentric passages of the binary and in turn the number of peaks in the cooling rate and X-ray light curves occurring over a given period of time. The number of shifts in wavelength space noticeable in the $H\alpha$ trailed spectrogram would also change, reflecting the change in the orbital period of the binary. This may complicate the prediction and observational followup of the outbursts, since after the first few orbital cycles the uncertainty in the orbital period of the binary will be rather large (weeks to months; see the example of OJ 287). If a decrease in the orbital period of a MBHB candidate can be determined from the observed light curves, it would imply that the binary is dissipating orbital angular momentum

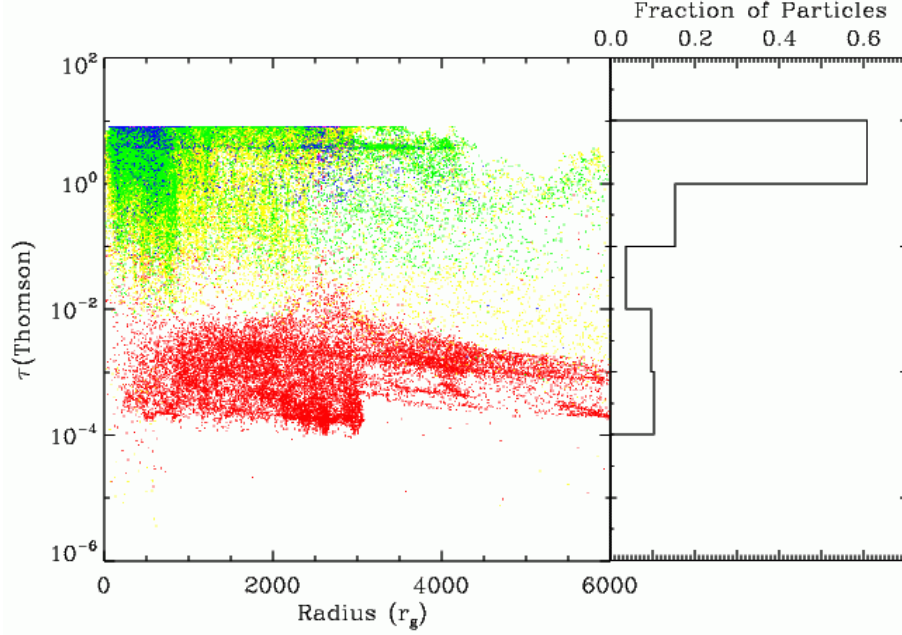


FIG. 22.— *Left:* Optical depth to Thomson scattering of each gas cell as a function of radius, at a time of 9.4 years in S-model. This figure corresponds to the morphology of the disk as plotted in panel 2 of Figure 7. *Right:* Histogram showing the fraction of particles as a function of Thomson optical depth.

via interactions with the gas disk or emission of gravitational waves.

The MBHBs likely to be discovered by monitoring of light curves and H α emission line profiles of candidate galaxies would likely have orbital periods of order of 10 yr or less, implying binaries with subparsec orbital separations. The dominant dissipation mechanism could be determined if a constraint on the masses of black holes can be put in addition to the rate of change of the orbital period. One could then compare the observed rate of inspiral to that predicted by the theory of general relativity for some assumed eccentricity; if the two are discrepant this could be explained by presence of the gaseous dynamical friction.

Structure of the disk. Besides the total mass, the efficiency of dynamical friction depends on the structure of the accretion disk. The intensity of the gas drag is stronger in systems where the density of the gas is higher and where a massive body moves supersonically with respect to the ambient medium (Östriker 1999). The structure of nuclear accretion disks on a subparsec scale is rather uncertain and in our calculations we assumed that the disk is geometrically thin. The results from the larger scale simulations by Escala et al. (2005) and Mayer et al. (2006a) provide useful insights into the effect that a different equation of state of the gas disk can have on the orbital decay of the binary at separations of 10–100 pc. Both groups find that the binary inspiral is more efficient in galactic disks with less pressure support and smaller scale heights. Such disks resemble clumpy and dense disks in starforming galaxies. In addition, Mayer et al. (2006a) find that for a galactic merger to result in a bound pair of massive black holes and eventually a coalescence within the Hubble time, the AGN should not play an important role as a source of heat in the disk during the merger phase.

Role of starburst and AGN. A number of authors found

that when a large fraction of the disk gas is funneled to the central 1 kpc, following a galactic merger, it can lead to nuclear starburst on timescale less than 10^8 yr (Barnes & Hernquist 1996; Di Matteo, Springel, & Hernquist 2005; Springel, Di Matteo, & Hernquist 2005). Because it may take 10^7 yr or longer for a binary to sink from kiloparsec to subparsec scales, the MBHB inspiral and coalescence in such galaxies may coincide with an active starburst (Dotti et al. 2006b). It appears that if a starburst reaches its peak before the MBHB merges, a large fraction of the gas may be already turned into stars while the remaining gas will be exposed to the starburst feedback, thus diminishing the role of gas as a dissipation agent in the MBHB inspiral. The resulting accretion rate onto the black holes may be too low to give rise to observable signatures in the form of periodic outbursts and variable H α emission line profiles; these galaxies would appear as ultraluminous or luminous starburst galaxies (Fabian et al. 1998; Dotti et al. 2006b). However, if the onset of a strong AGN activity in either of the parent nuclei precedes the starburst, the mechanical and radiative feedback could inhibit both the starburst and further accretion onto the black holes and thus suppress the electromagnetic signatures of the binary.

Model of radiation physics. Since a fully 3D radiative transfer calculation has not been developed yet the model of radiation physics that is employed here relies on several assumptions. Here we address the key assumptions that can directly affect the balance between heating and cooling in the simulation, and consequently the electromagnetic signatures of the binary system. The first assumption is related to the covering factor, ζ , used to parametrize the effects of self-shielding and geometry when gas is illuminated by the incident radiation (equation 13). In our calculation this coefficient has a fixed

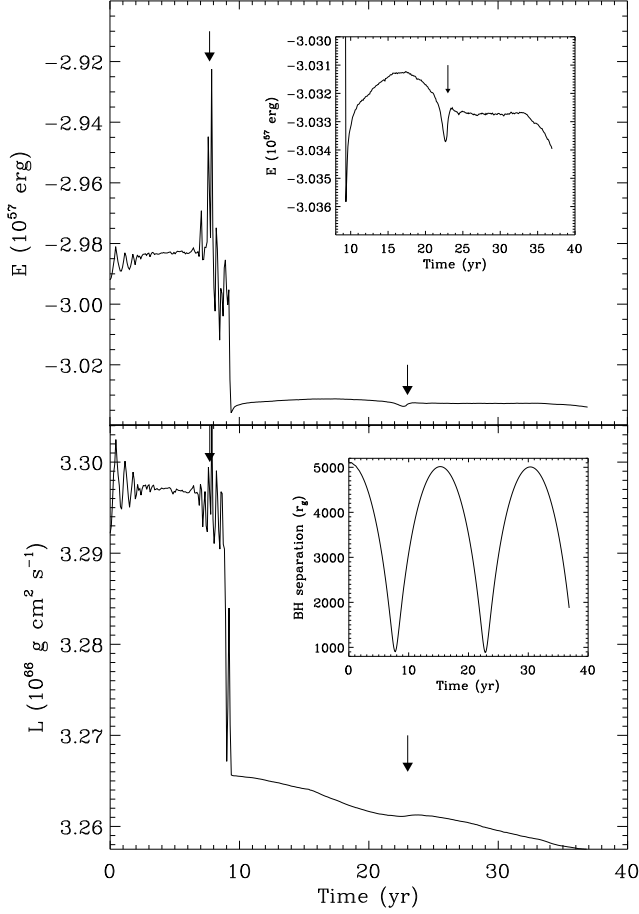


FIG. 23.— *Top*: Evolution of the binding energy of the binary over two orbits in the BB-model. *Inset*: Binding energy in the period 10 to 40 yr in more detail. *Bottom*: Evolution of the orbital angular momentum of the binary. The arrows mark the times of pericentric passages of the binary. *Inset*: Evolution of the orbital separation of the binary.

value while realistically it is a function of time and the position of a particle with respect to the source of illumination. Varying ζ would result in a different temperature in the gas hence, different amounts of hot and cold components of gas. For example, a larger value of ζ would amount in an increase of the diffuse, hot component of gas. This would boost the $H\alpha$ and X-ray luminosities but may not affect significantly the conclusions about the variability of these components. Alternatively, a smaller value of ζ would result in more gas being in the cold phase and confined to the plane of the disk. In this scenario both the $H\alpha$ and X-ray luminosities would be lower, and the $H\alpha$ light could also exhibit a periodicity. This is because the colder and denser gas is more susceptible to shocks induced by the secondary black hole.

Another important assumption in our calculation is that radiative cooling of the gaseous accretion disk can be approximated by a sum over the discrete gas particles. Each particle represents a gas cell of mass $0.1 M_\odot$. The approximation should converge to an exact solution when $N_{part} \rightarrow \infty$ in case when the gas is optically thin to radiation. We thus conclude that for the diffuse gas component in our simulations this approxima-

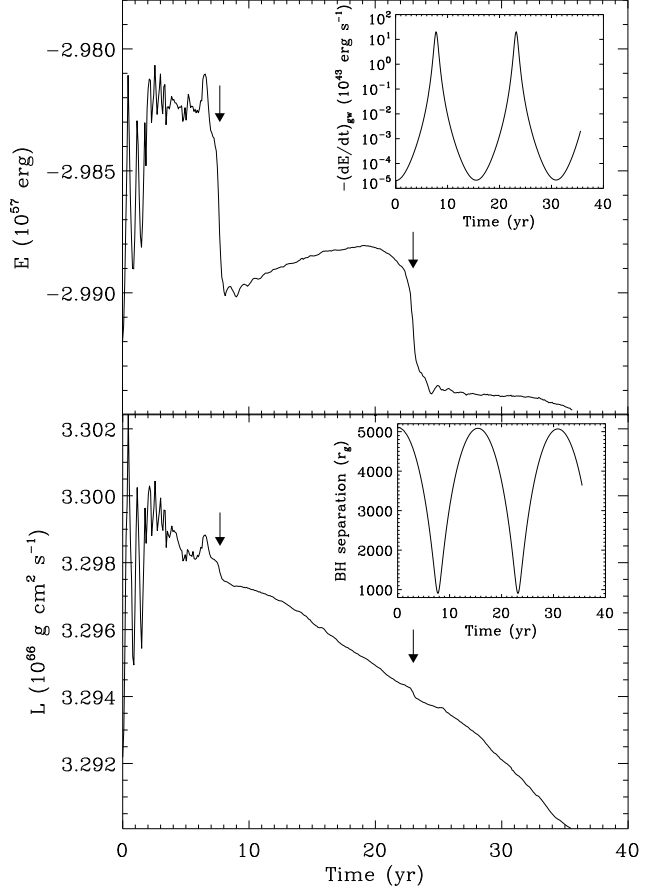


FIG. 24.— Similar to previous figure, except for the S-model. *Top inset*: Energy loss rate due to emission of gravitational waves over time. The binary loses orbital energy via gravitational waves at a mean rate of about $7 \times 10^{42} \text{ erg s}^{-1}$ and emits with the highest rate close to the pericenter. *Bottom inset*: Evolution of the orbital separation of the binary.

tion should be a satisfactory description and we turn attention to the optically thick component. This component has a higher neutral hydrogen column density (Figure 21) and is confined to a disk with the thickness corresponding to one smoothing length, h_{sml} . Therefore, the vertical structure of the disk is not resolved and every gas cell within the disk should cool by emission from the top and bottom of its surface. This is equivalent to a geometrically thin and optically thick accretion disk model where gas cools by emission from the two faces of the disk. In our model the gas cells radiate isotropically, over their entire surface area and according to the cooling rate per unit area determined by *Cloudy*. Thus we overestimate the total cooling from the optically thick component of gas by a factor of approximately 2. The largest error is expected for the BB-model, where all gas particles are assumed to be optically thick, while the S and SR models should provide a more accurate description.

Role of resolution. Increasing the resolution yields a better accuracy in the calculation of angular momentum transport and at the same time it may cause larger errors in the treatment of cooling in our models. We chose 100k particles for the BB, S, and SR models and carried out several tests in order to assess the role of reso-

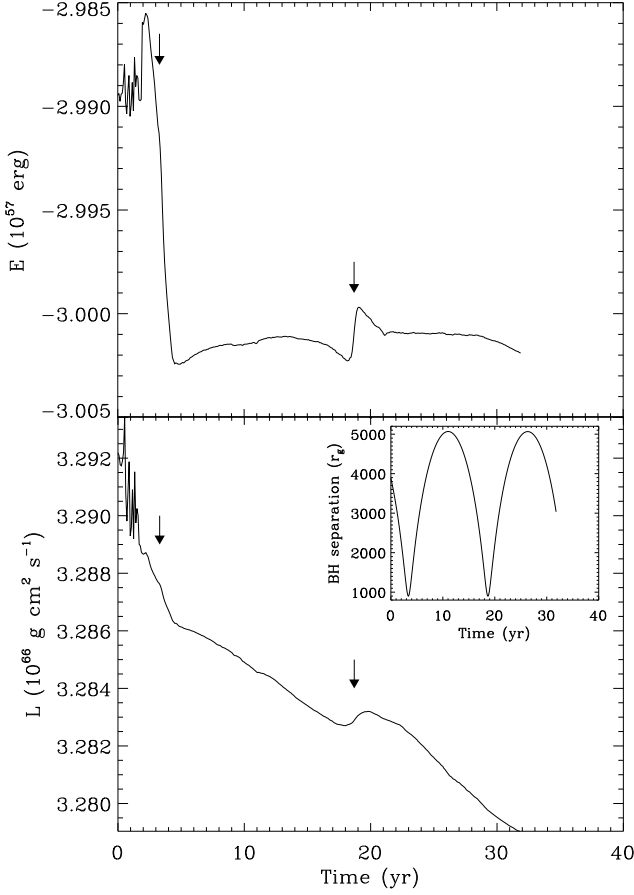


FIG. 25.— Similar to previous figure, except for the SR-model.

lution in the heating, cooling, and evolution of angular momentum in our simulations. The first set of tests is carried out by evolving the initial conditions (the IC-runs, see Table 2), with the primary black hole and the solar metallicity gas disk, before the secondary black hole is introduced. Thus we can isolate the dependence of angular momentum transport and cooling on resolution, in absence of shocks. The results of the three runs, IC1, IC2, and IC3 with 20k, 100k, and 500k particles, respectively, are shown in Figures 26 and 27, after the initial conditions were evolved for 8 years. The evolution of angular momentum appears strongest in the 20k run where the pressure gradient drives the evolution of the surface density at the inner disk radius (see the top panel of Figure 26) while at larger radii the distributions appear consistent. The dominant component of pressure is thermal gas pressure; the viscous pressure is of lesser importance and it operates on much longer time scales. The accretion disks at lower resolution thus appear to have more gas pressure support than at higher resolution. Lower resolution also results in more viscous disks and shorter viscous time scales, as shown in middle panel of Figure 26 where we plot the viscous time scale, $\tau_{\text{viscous}} \sim r^2 / (\alpha_{\text{Gadget}} h_{\text{sml}} c_s)$.

The bottom panel of Figure 26 shows the temperature profile of the disk calculated at three different resolutions, from the same snapshot in time. The disk in the 500k IC3 is the coldest compared to the 100k IC2

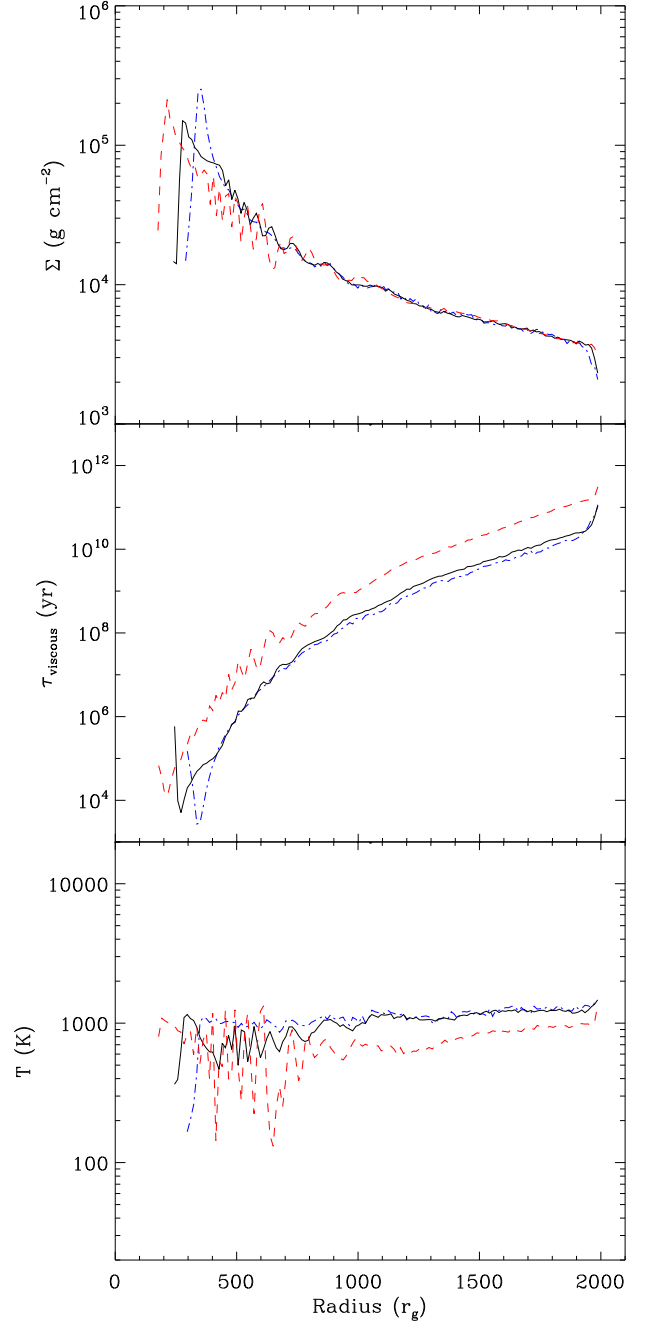


FIG. 26.— The effect of resolution on the disk surface density (top), the viscous time scale (middle), and the temperature profiles (bottom) in models, where the secondary black hole was not introduced to the simulation. The profiles shown are for runs 20k IC1 (dash-dot, blue line), 100k IC2 (solid, black line), and 500k IC3 (dashed, red line), all at a time of 8 years after the beginning of a simulation. The gas was assumed to have a solar metallicity. See discussion in § 4 for more details.

and 20k IC1 runs. This is a consequence of the dependence of the cooling model on the resolution. In the solar metallicity models, the disk cooling rate is expected to scale with the total number of gas particles and their emitting volume as $\propto N_{\text{part}} h_{\text{sml}}^3 = \text{const.}$ Figure 27 shows the cooling curves of an unperturbed, passively cooling disk for the three runs with the cooling being strongest in the 500k one. The scaling notably departs from the analytical expectation because

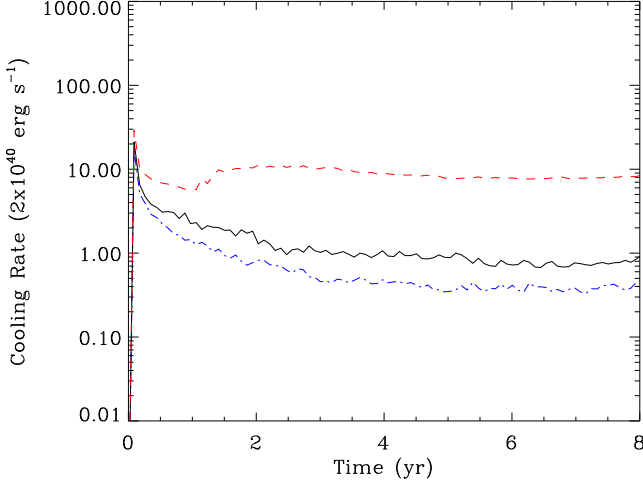


FIG. 27.— Dependence of the cooling rate on resolution in a model where the secondary black hole is absent and the solar metallicity gas disk is cooling passively. The curves are from runs 20k IC1 (dash-dot, blue line), 100k IC2 (solid, black line), and 500k IC3 (dashed, red line), at the time 8 years after the beginning of each simulation.

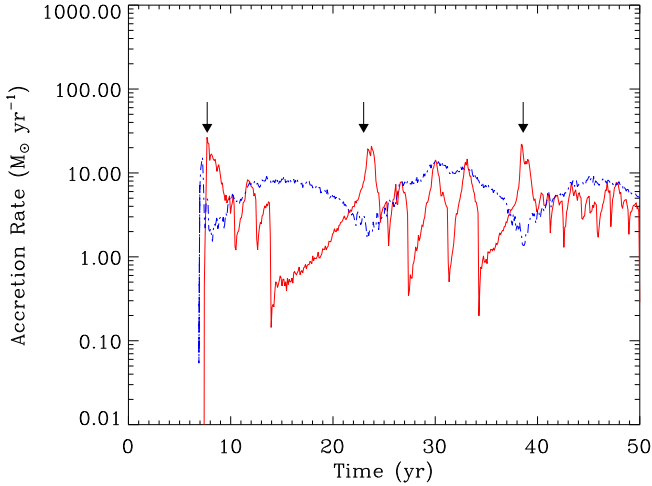


FIG. 28.— Effective accretion rate on the primary (solid, red line) and secondary (dashed, blue line) black holes calculated from the 20k S1 run, a lower resolution equivalent of the 100k S-model run (Figure 10). Note that this model has been run for a longer time (close to 3 orbital periods) and that three peaks are noticeable in the accretion curve. The arrows mark the times of pericentric passages of the binary.

the adaptive smoothing length, h_{sml} , does not decrease with the resolution as quickly as $\sim N_{part}^{-1/3}$. Consequently, the higher resolution runs are characterized by a larger cooling volume with respect to the lower resolution ones. Because the cooling rate of a black-body emitter is characterized by its emitting surface area, rather than volume, the dependence of the cooling on resolution is different in the BB-model. In this case the cooling rate is nominally expected to increase with resolution as $\propto N_{part} h_{sml}^2 \sim N_{part}^{1/3}$ (see S 2.3). However, the cooling rate may have stronger dependence on N_{part} due to the behavior of h_{sml} with resolution, as described previously for the solar metallicity case.

In order to estimate how much the cooling rates measured from our simulations suffer from the systematics discussed in this section, we compare the cooling rates for the passively cooling disk from the IC runs with the analytically calculated cooling rate for a black body with $T = 1000\text{K}$ and surface area equal to that of the disk. The comparison is meaningful because the cold, nearly isothermal, optically thick and geometrically thin disk can be described as a black body until it is perturbed or illuminated. We obtain a cooling rate of $L_{bb} = 3 \times 10^{41} \text{ erg s}^{-1}$, which is slightly higher but within an order of magnitude of the cooling rate in the 100k IC2 run (Figure 27). The same is true for the early portions of the cooling curves in the BB, S, and SR models, before the passage of the secondary through the disk (Figures 6, 9, and 13). Their difference from the analytic estimate value can be explained by slight departures of the temperature of the gas particles from 1000K. We conclude that the cooling rates calculated in our models with 100k particles are in fair agreement with the analytic estimate in the limit of an optically thick gas disk. We also discuss a possibility for further improving the BB cooling model and suppress the dependence of cooling on resolution in § 4.1.

In the second set of tests we examine the effect of resolution on the accretion rates and the variable $H\alpha$ emission line profiles in the presence of the secondary black hole. These quantities are connected to the resolution through the graininess of the gas and through the artificial viscosity, which leads to different results for shocks. For the purpose of the test we carried out the S1 simulation of the binary with a prograde disk using 20k particles (analogous to the 100k S model). The accretion rate curves (Figure 28) show the same prominent features as the ones in the 100k S-model (Figure 10). The total accretion rate in the 20k S1 run is in the range $1 - 10 M_{\odot} \text{ yr}^{-1}$ and is slightly higher than in the 100k S run. In the lower resolution run the contrast between the accretion rate of the secondary black hole at pericenter and apocenter appears higher, creating pronounced periodic humps in the accretion curve. This is likely the result of the Bondi-like accretion on the secondary coupled with a lower particle number density in the 20k S1 run.

In addition, we calculate the $H\alpha$ emission line profiles from the 20k S1 run in the same way as in the S model; the results are shown in Figure 29. As a consequence of the lower cooling in the 20k run, the intrinsic intensity of the $H\alpha$ lines is several times lower than in the 100k S-model run but the integrated $H\alpha$ luminosity is the same, $L_{H\alpha} \sim 10^{40} \text{ erg s}^{-1}$. This can be understood having in mind that while the intrinsic line intensity decreases at lower resolutions, the smoothing radius used to estimate the emitting surface of a gas particle, increases, and the two effects cancel out in calculation of luminosity. The shape and width of the profiles show the same dominant features as the profiles in 100k S-run and do not appear to be very sensitive to the change of resolution.

While employing a higher number of particles has a clear advantage we find that a satisfactory accuracy is achieved with 100k particles given the time scales in-

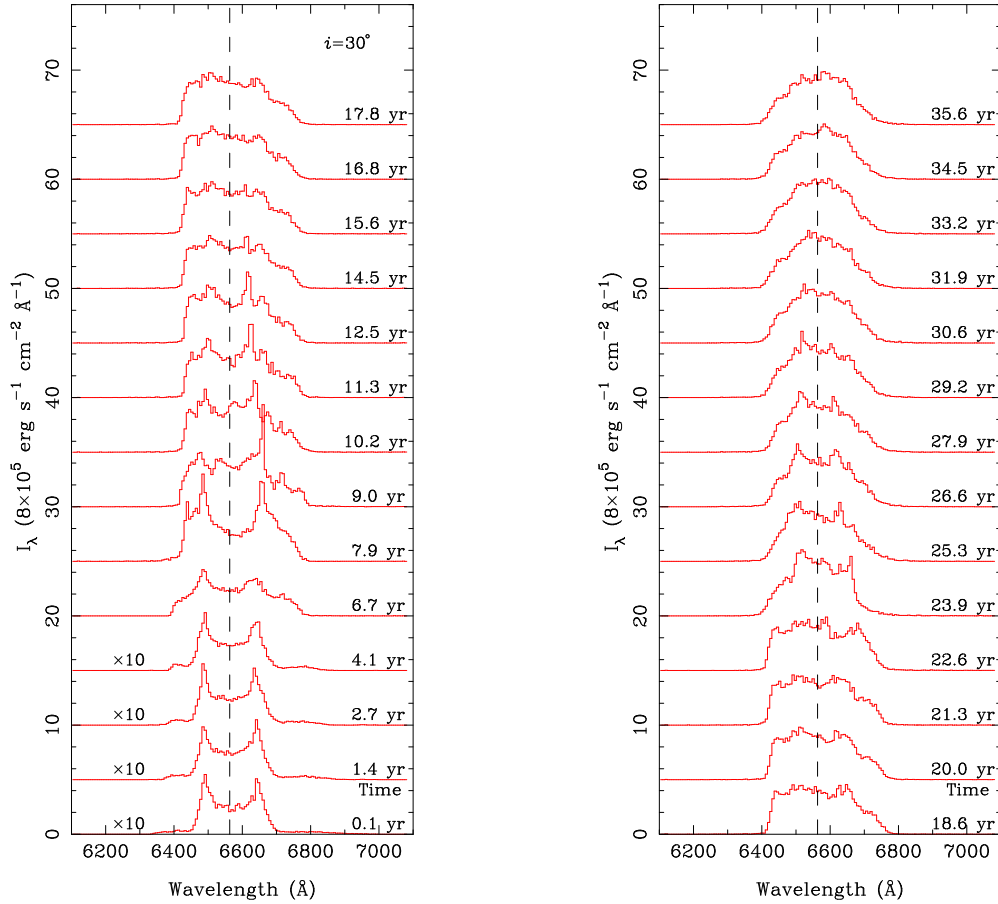


FIG. 29.— Sequence of H α emission line profiles calculated from the 20k S1 run, a lower resolution equivalent of the 100k S-model run. The emission line profiles are plotted for the same time slices as in Figure 17, for comparison. Note the lower intensity scale for the profiles in 20k S1 run but otherwise very similar profile widths and shapes to those in 100k run. The inclination of the plane of the disk with respect to the observer is as marked on the figure. The vertical dashed line at 6563 Å marks the H α rest frame wavelength.

volved in our simulations. The evolution of angular momentum in the 100k runs is slow and the viscous evolution even slower and they do not result in shocks and transients in the gas. The estimated systematic error in cooling rate due to the dependence on resolution is within one order of magnitude and the shapes of the H α emission line profiles appear robust.

Role of accretion model. In the last paragraph of § 2 we describe the approximation we used in order to estimate the accretion rates of the two black holes given the properties of their perturbed but unresolved accretion flows. We tested whether the accretion rate onto the secondary black hole affects the results by lowering it by a factor of 100 in one of the models. We refer to this as the S2-model. From this run, in which we employed 20k particles, we calculated the observational signatures and found that they are very similar to the 20k S1 and 100k S-models (specifically, the cooling curve features and periodicity, H α profiles, and H α light curve). The implication is that varying the accretion rate efficiency of the secondary black hole with respect to that of the primary has a weak effect on the resulting observational signatures. As long as the primary black hole maintains equal or higher accretion rate than the secondary, the latter can be regarded as a passive perturber. We also note that the estimates of accretion rates in both accretion models are rather conservative, thus it

is more likely that we underestimate rather than overestimate the accretion rate.

In our simulations we modeled the binary with the semi-major axis of 0.015 pc, in the regime when the dissipation due to the gaseous background is still dominant over the gravitational radiation. This regime corresponds to the disk-driven migration stage in the 2D grid simulations of a binary and locally isothermal disk by Armitage & Natarajan (2002, hereafter, AN). Because there is an overlap in the scales treated by our respective simulations we compare the results of the two works. Note that in our simulations the binary orbit is assumed to be elliptical and the disk surface density initially corresponds to $\sim 10^5 \text{ g cm}^{-2}$ at the distance of $100r_g$ from the primary, in comparison to the circular orbit and the surface density of $\sim 10^6 \text{ g cm}^{-2}$ in AN. We find that the low density quasi-spherical outflow in our models reaches the scale of 1 pc in about 40 years, implying the outflow velocities of $\sim 10^4 \text{ km s}^{-1}$, in agreement with the prediction of AN. Unlike AN, we find that in the phase of the disk-driven migration the accretion rate of the primary is higher than the rate expected in the absence of a binary. The rate expected in the latter case is $\sim 10^{-3} M_\odot \text{ yr}^{-1}$ while the rate measured from our simulations $\geq 10^{-2} M_\odot \text{ yr}^{-1}$. We attribute this difference to a temperature distribution of the gas and the eccentric binary orbit. In our simulations, in general case, different gas phases can be found to reside at the same radii in the disk (Figures 8

and 12). The cold component of gas at $T \sim 10^3$ K is mostly confined to the plane of the binary orbit where it gets swept by the secondary black hole during every passage through the disk and accreted. In addition, a binary on an eccentric orbit effectively perturbs the accretion disk and drives the spatially extended high velocity outflows. The outflows carry away the excess angular momentum, allowing the gas at the innermost region of the disk to be accreted.

4.1. Future Prospects

The physical parameter space of a binary and gas disk system is very large and a thorough parameter study is beyond the scope of this paper. In the future it will be useful to investigate systems with different mass ratios in which the binary orbit and gaseous disk are not coplanar. In these systems the secondary black hole does not gradually migrate through the plane of the disk but crosses through the disk at some inclination. Consequently, such encounters are expected to have unique emission signatures. The next, even more general set of systems to be studied are binaries with two gas disks at different relative inclinations.

Because the model of radiation physics plays a decisive role in determining the character of the observational signatures, we outline a possible avenue for future improvement of the BB-model. Introducing a flux-limited diffusion approximation (Cleary & Monaghan 1999; Whitehouse et al. 2005; Mayer et al. 2006b) can offer a more accurate treatment of the optically thick component of gas by emulating a continuous diffuse radiation field in the inter-particle space. In this approximation the SPH particles which are embedded within some gas distribution diffuse heat to their neighbor particles as determined by the temperature gradient and coefficient of diffusion. The particles defining a surface boundary of an emitting region in addition to diffusion can freely radiate as a black-body or according to some other prescription. The main challenge in the implementation is determining which gas particles are constituents of the boundary layer in general case, when the normal of an emitting surface is not aligned with any preferred axis in the system and when its orientation varies in space and time (see Mayer et al. 2006b, for the case of a disk geometry).

Because our simulations are computationally expensive, we were not able to follow the longer-term evolution of the binary and the disk on time scales on which a gap is expected to form in the disk. The gap is a low density region that forms at the center of an accretion disk, on a scale comparable to that of the binary orbit, as a consequence of tidal torques that the binary exerts on the disk (Lin & Papaloizou 1979a,b). While we observed a lower peak density in the innermost region of the disk at the end of simulations, whether a gap in the disk is efficiently cleared or continuously replenished by the gas will depend on the gas temperature and hence, on the treatment of heating and cooling. The simple, exploratory models described here can be of importance in cases when the gap is either replenished or its formation process is not efficient. However in the future we will explore models in which the gap has already formed in the disk and investigate its implications for the accretion rates and observational signatures.

5. SUMMARY AND CONCLUSIONS

We developed a method for calculation of the observational signatures of MBHBs with an associated gas component. The method comprises SPH calculations carried out with a modified version of the code *Gadget* coupled with calculations of cooling and heating of the gas. We implemented and tested two different schemes for heating and cooling of gas in which the gas is described as a black-body emitter or a photoionized gas with solar composition. In the solar metallicity model heating and cooling of the gas are pre-calculated with the photoionization code *Cloudy*, along with the emission efficiency of the $H\alpha$ line, the optical depth to Thomson scattering, and the neutral hydrogen column density. This information allows

us to calculate the $H\alpha$ light curves and $H\alpha$ emission line profiles from this system.

Since MBHBs may spend the largest fraction of their lives at sub-parsec scales (Begelman et al. 1980) it is particularly interesting to study the observational signatures of such binaries. In this paper we investigated the electromagnetic signatures of binaries based on a few exploratory models; we outline the most important findings below:

- Based on the first set of models, presented here, we find that the X-ray outbursts should occur during pericentric passages of a coplanar binary. We suggest that periodic X-ray outbursts should persist as long as there is a supply of gas that the MBHB can interact with. A calculation of a much larger number of binary orbits is needed in order to confirm that the periodic outbursts are a long lived signature of the binary. At the estimated level of X-ray luminosity the binary systems interacting with the gas should be observable to a redshift of $z \leq 2$.
- Except for the recurrent outbursts in the X-ray light curve the signature of a binary is most easily discernible in the $H\alpha$ emission line profiles. The variable shape of the broad $H\alpha$ emission line profiles can be used as a first indicator when searching for MBHBs in the nearby universe, within 100 Mpc. Once the binary candidates are selected from a large spectroscopic survey (e.g., the SDSS) they can be monitored over long time intervals to look for the time-dependent signature of a binary. Based on our simulations (for a mass ratio of 0.1), the wavelength shift in the $H\alpha$ emission lines over the course of an orbital period should be measurable. If one can follow the regular variations of the line over a few cycles, one could constrain the properties of the binary, such as orbital period and the binary mass ratio.
- The observed signatures predicted here arise from the gas disk and accretion onto the two nuclei, both of which may not be detectable in galaxies where the nuclear region is obscured or gas exhausted by the star-

burst. The resulting signatures are in addition sensitive to the adopted model of radiation physics but are not very sensitive to the number of particles employed in the SPH simulations.

- The evolution of the intermediate phase binaries considered here is driven by interactions of the black holes with the accretion disk gas, while the emission of gravitational waves is secondary (3–4 orders of magnitude lower). Orbital energy is dissipated primarily via dynamical friction against the gaseous background and tidal torques in case of a binary co-rotating with the disk. In case of a counter-rotating binary, the tidal torques play the dominant role in the dissipation since dynamical friction becomes ineffective.
- The current limitation of the numerical method used in this study is that the calculation of a large number of orbits following the hydrodynamics and radiative heating and cooling becomes prohibitively expensive. Therefore, we are only able to model the observational signature of the system for a brief period of its evolution, after we have assumed a specific initial configuration.

If the signatures of binaries are found in observations, they could be used to estimate the number of MBHBs in this evolutionary stage and whether MBHBs indeed evolve quickly through the last parsec. Although the intermediate phase binaries themselves emit gravitational waves at frequencies too low to be detected with *LISA* their discovery is important for understanding the evolution of the diverse supermassive black hole binary population.

T.B. acknowledges the support of the Center for Gravitational Wave Physics at Penn State and the Zaccheus Daniel Fellowship. T.B. also wishes to thank Miloš Milosavljević and M. Coleman Miller for insightful discussions. The simulations of binaries and gas were carried out on computational cluster Pleiades at the Pennsylvania State University. We wish to thank the referee for detailed and thoughtful comments.

REFERENCES

- Aarseth, S. J. 2003, *Ap&SS*, 285, 367
 Armitage, P. J. & Natarajan, P. 2002, *ApJ*, 567, L9
 Armitage, P. J., & Natarajan, P. 2005, *ApJ*, 634, 921
 Baker, J. 2003, *Classical and Quantum Gravity*, 20, 201
 Balsara, D. S. 1995, *Journal of Computational Physics*, 121, 357
 Barnes, J. E. & Hernquist, L. 1992, *ARA&A*, 30, 705
 Barnes, J. E. & Hernquist, L. 1996, *ApJ*, 471, 115
 Bate, M. R., Bonnell, I. A., & Bromm, V. 2003, *MNRAS*, 339, 577
 Begelman, M. C., Blandford, R. D., & Rees, M. J. 1980, *Nature*, 287, 307
 Begelman, M. C. & Rees, M. J. 1978, *MNRAS*, 185, 847
 Bender, P. L. 1998, *Eighteenth Texas Symposium on Relativistic Astrophysics*, 536
 Black, J. H. 1981, *MNRAS*, 197, 553
 Bromm, V. & Loeb, A. 2003, *ApJ*, 596, 34
 Capetti, A., Zamfir, S., Rossi, P., Bodo, G., Zanni, C., & Massaglia, S. 2002, *A&A*, 394, 39
 Cen, R. 1992, *ApJS*, 78, 341
 Centrella, J. M. 2003, *AIP Conf. Proc.* 686: The Astrophysics of Gravitational Wave Sources, 686, 219
 Cleary, P. W. & Monaghan J. J. 1999, *J. Comp. Phys.*, 148, 227
 Collin-Souffrin, S. & Dumont, A.M. 1989, *A&A*, 213, 29
 Danzmann, K. & the LISA study team 1996, *Classical and Quantum Gravity*, 13, A247
 De Paolis, F., Ingrassio, G., & Nucita, A. A. 2002, *A&A*, 388, 470
 De Paolis, F., Ingrassio, G., Nucita, A. A., & Zakharov, A. F. 2003, *A&A*, 410, 741
 Di Matteo, T., Springel, V., & Hernquist, L. 2005, *Nature*, 433, 604
 Dotti, M., Colpi, M., & Haardt, F. 2006a, *MNRAS*, 367, 103
 Dotti, M., Salvaterra, R., Sesana, A., Colpi, M., & Haardt, F. 2006b, *MNRAS*, 372, 869
 Dotti, M., Colpi, M., Haardt, F., & Mayer, L. 2006c, *MNRAS*, submitted (astro-ph/0612505)
 Eracleous, M., & Halpern, J. P. 2003, *ApJ*, 599, 886
 Eracleous, M., Halpern, J. P., & Livio, M. 1996, *ApJ*, 459, 89
 Eracleous, M., Halpern, J. P., Gilbert, A. M., Newman, J. A., & Filippenko, A. V. 1997, *ApJ*, 490, 216
 Escala, A., Larson, R. B., Coppi, P. S., & Mardones, D. 2004, *ApJ*, 607, 765
 Escala, A., Larson, R. B., Coppi, P. S., & Mardones, D. 2005, *ApJ*, 630, 152
 Etherington, J., & Maciejewski, W. 2006, *MNRAS*, 367, 1003
 Fabian, A. C., Barcons, X., Almaini, O., & Iwasawa, K. 1998, *MNRAS*, 297, L11
 Fan, J. H., Xie, G. Z., Pecontal, E., Pecontal, A., & Copin, Y. 1998, *ApJ*, 507, 173
 Ferland, G. J., Korista, K. T., Verner, D. A., Ferguson, J. W., Kingdon, J. B., & Verner, E. M. 1998, *PASP*, 110, 761
 Ferland, G. J. 2003, *ARA&A*, 41, 517
 Gaskell, C. M. 1983, *Quasars and Gravitational Lenses*, 473
 Gaskell, C. M. 1996, *Lecture Notes in Physics*, Berlin Springer Verlag, 471, 165
 Gould, A. & Rix, H. 2000, *ApJ*, 532, L29
 Haehnelt, M. G. 1994, *MNRAS*, 269, 199
 Haehnelt, M. G. & Kauffmann, G. 2002, *MNRAS*, 336, L61

- Halpern, J. P. & Filippenko, A. V. 1988, *Nature*, 331, 46
- Halpern, J. & Filippenko, A. 1992, *Testing the AGN Paradigm*, 57
- Hemsendorf, M., Sigurdsson, S., & Spurzem, R. 2002, *ApJ*, 581, 1256
- Hernquist, L., & Katz, N. 1989, *ApJS*, 70, 419
- Hollenbach, D., & McKee, C. F. 1979, *ApJS*, 41, 555
- Hudson, D. S., Reiprich, T. H., Clarke, T. E., & Sarazin, C. L. 2006, *A&A*, 453, 433
- Hughes, S. A. 2002, *MNRAS*, 331, 805
- Hunstead, R. W., Murdoch, H. S., Condon, J. J., & Phillips, M. M. 1984, *MNRAS*, 207, 55
- Ivanov, P. B., Papaloizou, J. C. B., & Polnarev, A. G. 1999, *MNRAS*, 307, 79
- Katz, N., Weinberg, D. H., & Hernquist, L. 1996, *ApJS*, 105, 19
- Kazantzidis, S., et al. 2005, *ApJ*, 623, L67
- Kocsis, B., Frei, Z., Haiman, Z., & Menou, K. 2006, *ApJ*, 637, 27
- Komossa, S., Burwitz, V., Hasinger, G., Predehl, P., Kaastra, J. S., & Ikebe, Y. 2003a, *ApJ*, 582, L15
- Komossa, S. 2003b, *AIP Conf. Proc.* 686: *The Astrophysics of Gravitational Wave Sources*, 686, 161
- Kormendy, J. & Richstone, D. 1995, *ARA&A*, 33, 581
- Landau, L. D., & Lifshitz, E. M. 1975, *The classical theory of fields*, Heinemann, Oxford
- Leahy, J. P. & Williams, A. G. 1984, *MNRAS*, 210, 929
- Lee, W. H., & Kluźniak, W. Ł. 1999, *MNRAS*, 308, 780
- Lehto, H. J. & Valtonen, M. J. 1996, *ApJ*, 460, 207
- Li, Y., Mac Low, M.-M., & Klessen, R. S. 2005, *ApJ*, 626, 823
- Lin, D. N. C., & Papaloizou, J. 1979, *MNRAS*, 186, 799
- Lin, D. N. C., & Papaloizou, J. 1979, *MNRAS*, 188, 191
- Liu, F. K. 2004, *MNRAS*, 347, 1357
- Liu, F. K., Wu, X., & Cao, S. L. 2003, *MNRAS*, 340, 411
- Liu, F. K., & Wu, X.-B. 2002, *A&A*, 388, L48
- MacFadyen, A. I., & Milosavljević, M. 2006, in prep. (astro-ph/0607467)
- Mayer, L., Kazantzidis, S., Madau, P., Colpi, M., Quinn, T., & Wadsley, J. 2006a, to appear in the *Proceedings of the "Relativistic Astrophysics and Cosmology - Einstein's Legacy"* (astro-ph/0602029)
- Mayer, L., Lufkin, G., Quinn, T., & Wadsley, J. 2006b, submitted to *ApJ*(astro-ph/0606361)
- Menou, K., Haiman, Z., & Narayanan, V. K. 2001, *ApJ*, 558, 535
- Merritt, D. 2002, *ApJ*, 568, 998
- Merritt, D. & Ekers, R. D. 2002, *Science*, 297, 1310
- Mihos, J. C. & Hernquist, L. 1996, *ApJ*, 464, 641
- Milosavljević, M. & Merritt, D. 2001, *ApJ*, 563, 34
- Milosavljević, M. & Merritt, D. 2003, in *AIP Conf. Proc.* 686, *The Astrophysics of Gravitational Wave Sources*, ed. J. Centrella (New York: AIP), 201
- Milosavljević, M., & Phinney, E. S. 2005, *ApJ*, 622, L93
- Monaghan, J. J. 1992, *ARA&A*, 30, 543
- Monaghan, J. J. 1997, *Journal of Computational Physics*, 136, 298
- Ostriker, E. C. 1999, *ApJ*, 513, 252
- Paczynsky, B. & Wiita, P. J. 1980, *A&A*, 88, 23
- Papaloizou, J. C. B., Nelson, R. P., & Masset, F. 2001, *A&A*, 366, 263
- Parma, P., Ekers, R. D., & Fanti, R. 1985, *A&AS*, 59, 511
- Perets, H. B., Hopman, C., & Alexander, T. 2006, *ApJ*, 656, 709
- Peterson, B. M. & Wandel, A. 2000, *ApJ*, 540, L13
- Quinlan, G. D. & Hernquist, L. 1997, *New Astronomy*, 2, 533
- Rhook, K. J., & Wyithe, J. S. B. 2005, *MNRAS*, 361, 1145
- Richstone, D., et al. 1998, *Nature*, 395, A14
- Rieger, F. M. & Mannheim, K. 2000, *A&A*, 359, 948
- Rodriguez, C., Taylor, G. B., Zavala, R. T., Peck, A. B., Pollack, L. K., & Romani, R. W. 2006, *ApJ*, 646, 49
- Roos, N., Kaastra, J. S., & Hummel, C. A. 1993, *ApJ*, 409, 130
- Saslaw, W. C., Valtonen, M. J., & Aarseth, S. J. 1974, *ApJ*, 190, 253
- Schoenmakers, A. P., de Bruyn, A. G., Röttgering, H. J. A., van der Laan, H., & Kaiser, C. R. 2000, *MNRAS*, 315, 371
- Sesana, A., Haardt, F., Madau, P., & Volonteri, M. 2004, *ApJ*, 611, 623
- Sesana, A., Haardt, F., Madau, P., & Volonteri, M. 2005, *ApJ*, 623, 23
- Sigurdsson, S. 1998, *AIP Conf. Proc.* 456: *Laser Interferometer Space Antenna*, Second International LISA Symposium on the Detection and Observation of Gravitational Waves in Space, 456, 53
- Sillanpää, A., Haarala, S., Valtonen, M. J., Sundelius, B., & Byrd, G. G. 1988, *ApJ*, 325, 628
- Shakura, N. I. & Sunyaev, R. A. 1973, *A&A*, 24, 337
- Springel, V., Yoshida, N., & White, S. D. M. 2001, *New Astronomy*, 6, 79
- Springel, V. 2005, *MNRAS*, 364, 1105
- Springel, V., Di Matteo, T., & Hernquist, L. 2005, *MNRAS*, 361, 776
- Starling, R. L. C., Siemiginowska, A., Uttley, P., & Soria, R. 2004, *MNRAS*, 347, 67
- Steinmetz, M. 1996, *MNRAS*, 278, 1005
- Strateva, I. V., et al. 2003, *AJ*, 126, 1720
- Sudou, H., Iguchi, S., Murata, Y., & Taniguchi, Y. 2003, *Science*, 300, 1263
- Sulentic, J. W., Marziani, P., & Dultzin-Hacyan, D. 2000, *ARA&A*, 38, 521
- Thorne, K. S. & Braginskii, V. B. 1976, *ApJ*, 204, L1
- Thoul, A. A. & Weinberg, D. H. 1996, *ApJ*, 465, 608
- Torres, D. F., Romero, G. E., Barcons, X., & Lu, Y. 2003, *ApJ*, 596, L31
- Valtaoja, L., Valtonen, M. J., & Byrd, G. G. 1989, *ApJ*, 343, 47
- Valtaoja, E., Teräsranta, H., Tornikoski, M., Sillanpää, A., Aller, M. F., Aller, H. D., & Hughes, P. A. 2000, *ApJ*, 531, 744
- Volonteri, M., Haardt, F., & Madau, P. 2003, *ApJ*, 582, 559
- Wandel, A., Peterson, B. M., & Malkan, M. A. 1999, *ApJ*, 526, 579
- Wang, T., Zhou, H., & Dong, X. 2003, *AJ*, 126, 113
- Whitehouse, S. C., Bate, M. R., & Monaghan, J. J. 2005, *MNRAS*, 364, 1367
- Wyithe, J. S. B., & Loeb, A. 2003, *ApJ*, 590, 691
- Xie, G. 2003, *Publications of the Yunnan Observatory*, 95, 107
- Yu, Q. 2002, *MNRAS*, 331, 935
- Zier, C. & Biermann, P. L. 2001, *A&A*, 377, 23
- Zier, C. & Biermann, P. L. 2002, *A&A*, 396, 91
- Zier, C. 2006, *MNRAS*, 371, L36